MDPI

Article

A Noble-Gas-Centered Coordinate for Within-Period Atomic Property Trends

Jonathan Washburn[1], Megan Simons[1] and Elshad Allahyarov[1,2,3,4,*]

[1] Recognition Physics Institute, Austin, Texas, USA
[2] Department of Physics, Case Western Reserve University, Cleveland, Ohio, USA
[3] Institut für Theoretische Physik II: Weiche Materie, Heinrich-Heine Universität Düsseldorf, Germany
[4] Theoretical Department, Joint Institute for High Temperatures, RAS, Moscow, Russia
* Correspondence: elshad.allakhyarov@case.edu

Abstract

We introduce a single dimensionless landscape function $J_{\mathrm{chem}}(\rho) = \cosh(\rho \ln \varphi) - 1$, with $\varphi = (1+\sqrt{5})/2$, defined on the noble-gas-centred coordinate $\rho = d/L_p \in [0,1)$, and show that it organizes four central within-period atomic observables, first ionization energy IE_1, electron affinity EA, Mulliken electronegativity χ_M, and Pearson chemical hardness η, on a single periodic-table axis. The outward step $\Delta J^{+}_{\mathrm{chem}}$ delivers IE_1, the inward gap $\Delta J^{-}_{\mathrm{chem}} = J_{\mathrm{chem}}(1) - J_{\mathrm{chem}}(\rho)$ delivers EA and η, and χ_M follows from Mulliken's identity. Benchmarked against NIST and Pearson tabulated atomic data, the framework reproduces the within-period IE_1 envelope across periods 2–6 and localizes every upward deviation on the textbook anomaly sites $\{p^3, d^5, f^7, s^2, d^{10}\}$; it yields two parameter-free golden-ratio ionization-energy identities ($\varphi^{1/4}$ on heavy noble-gas pairs and φ^2 on halogen/alkali pairs, agreeing with data to MAD $\approx 1\%$ and $\approx 5\%$); and it provides single-parameter analytical fits for EA (MAE 0.3–0.4 eV), Pearson hardness η, and Mulliken χ_M ($R^2 = 0.73$ on a 15-atom four-class benchmark). By assembling four periodic-table observables under one golden-ratio cosh coordinate, the construction provides a compact analytical reference against which relativistic and shell-anomaly corrections can be quantified.

Keywords: periodic table; theoretical chemistry; ionization energy; electron affinity; electronegativity; chemical hardness; golden ratio; symmetry of the periodic table

Received:
Revised:
Accepted:
Published:

Citation: Washburn, J.; Simons, M.; Allahyarov, E. A Noble-Gas-Centered Coordinate for Within-Period Atomic Property Trends. *Symmetry* **2026**, *1*, 0. https://doi.org/

1. Introduction

Within each period of the periodic table [1–4], first ionization energy decreases monotonically from the period-closing noble gas to the alkali metal, with upward bumps at half-filled and completed-subshell sites $\{p^3, d^5, f^7, s^2, d^{10}\}$. Electron affinity and Pearson chemical hardness show the same broad descent, with related anomaly structure. Mulliken electronegativity inherits the same broad trend because it is half their sum.

This paper asks whether two landscape steps derived from a single dimensionless function $J_{\mathrm{chem}}(\rho)$ on the noble-gas-centred coordinate $\rho = d/L_p \in [0,1)$- the outward step $\Delta J^{+}_{\mathrm{chem}}$ and the gap $\Delta J^{-}_{\mathrm{chem}} = J_{\mathrm{chem}}(1) - J_{\mathrm{chem}}(\rho)$, can organize IE_1, EA, and (via Mulliken's identity) χ_M, with η assigned the same kernel as EA. The function is the cosh form $J_{\mathrm{chem}}(\rho) = \cosh(\rho \ln \varphi) - 1$, with $\varphi = (1+\sqrt{5})/2$, established in Refs. [5,6] as the unique reciprocal cost on positive ratios under standard smoothness conditions (Appendix A).[1]

[1] The uniqueness statement and the φ-power identities used below are also formalized in Lean 4 in the Recognition Science library; see the Data Availability statement.

The present paper takes J_{chem} as a fixed analytical input and develops its empirical content on the periodic table.

The four observables are conventionally treated separately: IE_1 and EA from atomic spectroscopy and electronic-structure calculations [7–9]; electronegativity from empirical scales [10–15]; chemical hardness from derivative-based density-functional arguments [16–20]. For context, recent reviews on periodic-table form, shell filling, and relativistic extensions to superheavy atoms include Refs. [21–23]; the present work combines IE_1, EA, electronegativity, and chemical hardness in a single coordinate-based analysis.

Complementary modern perspectives on the structure and origin of chemical periodicity further motivate a coordinate-based view: the formal chemical-space and order-theoretic analysis of the periodic system by Leal and Restrepo [24], the explicit account of the physical origin of chemical periodicities across the elements by Cao, Hu, Li, and Schwarz [25], and the unsupervised machine-learning recreation of the periodic table from elemental property data by Kusaba et al. [26]. These works show, from data-analytic, physical, and machine-learning standpoints respectively, that the periodic regularities admit compact low-dimensional organizations; the single noble-gas-centred coordinate developed here is one such organization made fully analytical for four observables at once.

Two long-established quantitative pictures already organize the same within-period trends, and we use both as horizontal reference benchmarks throughout this paper. (i) The *effective-nuclear-charge (screening) model* of Slater and of Clementi and Raimondi [27–29] represents each electron as moving in a screened Coulomb field of charge $Z_{\mathrm{eff}} = Z - \sigma$, from which ionization energies and their ratios follow through $\mathrm{IE}_1 \propto Z_{\mathrm{eff}}^2/n^2$; this is the standard one-electron baseline for IE_1 and is closely related to the Koopmans/Hartree–Fock orbital-energy estimate [8]. (ii) *Conceptual density-functional theory* [16,17,19,30] defines electronegativity and chemical hardness as first and second derivatives of the electronic energy with respect to electron number, $\chi = -\partial E/\partial N$ and $\eta = \frac{1}{2}\,\partial^2 E/\partial N^2$, evaluated in practice by the finite-difference forms $\chi_M = \frac{1}{2}(\mathrm{IE}_1 + \mathrm{EA})$ and $\eta = \frac{1}{2}(\mathrm{IE}_1 - \mathrm{EA})$. The framework developed here is not a competitor to these established theories but a complementary single-coordinate organization, and Section 5.8 compares it directly against both the effective-nuclear-charge baseline (for the IE_1 ratios) and the conceptual-DFT hardness/electronegativity definitions (for η and χ_M).

The empirical content reduces to three IE_1 predictions and three derived checks. The IE_1 predictions are the heavy noble-gas ratio $\mathrm{IE}_1(G_p)/\mathrm{IE}_1(G_{p+1}) \approx \varphi^{1/4}$, the halogen-to-alkali ratio φ^2, and the within-period monotone IE_1 envelope with the standard anomaly sites flagged (Prediction 3, where periods 2–4 give 26 non-anomalous points on the monotone trend and 8 deviations at the textbook anomaly positions). The derived checks are a one-parameter EA fit across periods 4–6, a one-parameter Pearson-hardness fit across periods 2–4, and a single-parameter Mulliken-χ_M fit on 15 atoms across four chemical classes ($R^2 = 0.73$ globally, Section 5).

One closed-form expression $\Delta J^{-}_{\mathrm{chem}}(Z) = J_{\mathrm{chem}}(1) - J_{\mathrm{chem}}(d(Z)/L_p)$ is used for two observables: the EA proxy of Section 4.2 and the hardness predictor κ_{RS} of Section 4.4 (the functional-equation framework of Refs. [5,6]). The shared-kernel form unifies two observables under one analytical landscape gap with two independent per-period scales fitted against the EA and η data; the resulting ratio benchmark $\mathrm{EA}/\eta \approx C_{\mathrm{EA}}^{(p)}/C_{\eta}^{(p)}$ is confirmed by the period-4 NIST data with empirical mean matching the predicted constant to better than 1% (Section 5.7).

This paper proposes a compact phenomenological, coordinate-based framework that organizes broad within-period trends in IE_1, EA, χ_M, and η on a single analytical axis, and provides a useful baseline against which shell and relativistic corrections can be measured. The work is *not* an ab initio derivation of atomic structure, does *not* replace

electronic-structure theory, does *not* derive shell anomalies (which we identify post hoc with textbook sites), and does *not* provide a universal predictor without exclusions. Two of the headline ratio identities ($\varphi^{1/4}$ for heavy noble-gas IE, φ^2 for halogen/alkali IE) are empirical regularities consistent with the framework once a per-period absolute-energy scale E_p is admitted from data; a first-principles derivation of E_p is left to future work. "Prediction" in the rest of the paper refers to a model-derived ordering or proxy expression evaluated on a stated benchmark subset, not to a parameter-free quantitative forecast.

We state the theoretical status of the construction precisely, because it is intermediate between a purely empirical fit and a first-principles derivation. The *kernel* J is not an ad hoc choice: it is the unique reciprocal cost functional on positive ratios that satisfies a small set of standard regularity conditions (continuity, normalization, stationarity, positive curvature), proved in Refs. [5,6] and summarized in Appendix A; in that sense the cosh form has a theorem-level mathematical justification. What the framework does *not* yet derive from first principles are the two chemical modelling inputs identified explicitly in Section 3: the golden-ratio argument-rescaling φ, which is adopted as an ansatz, and the per-period absolute-energy scale E_p, which is fitted from data. The present paper therefore reports a theorem-backed kernel combined with two clearly labelled phenomenological inputs, and we regard the first-principles derivation of φ and E_p as the central open problem left for future work.

The paper is organized as follows. Section 2 fixes the notation. Section 3 constructs the landscape. Section 4 assigns the four observables to landscape steps. Section 5 presents the three IE_1 predictions and the EA, electronegativity, and hardness checks against NIST and Pearson data, and tests the shared-kernel ratio benchmark (Section 5.7). Section 6 states the conclusions.

2. Mathematical Setup

The symbols used throughout the paper are given in Table 1.

Table 1. Nomenclature used in the paper.

Symbol	Meaning
Z	Atomic number of the element under discussion.
G_p	Atomic number of the noble gas at the end of row p of the periodic table.
L_p	Length of row p, i.e. the number of elements in that row.
$d(Z)$	Number of electrons needed for element Z to reach the noble gas at the end of its row.
$v(Z)$	Position of the element within its row, counted from the alkali-metal side.
$\rho(Z)$	Normalized position in the row, defined as $d(Z)/L_p$.
$J_{\text{chem}}(\rho)$	Dimensionless landscape function used throughout the paper.
$\Delta J^{+}_{\text{chem}}$	Outward one-electron step: one electron farther from the noble-gas end of the row.
$\Delta J^{-}_{\text{chem}}$	Landscape gap to the fixed reference $J_{\text{chem}}(1)$: $J_{\text{chem}}(1) - J_{\text{chem}}(d/L_p)$. Used as both the EA proxy and the hardness predictor κ_{RS}.
χ_{struct}	Half-sum of the outward IE-step $\Delta J^{+}_{\text{chem}}$ and the EA-side gap $\Delta J^{-}_{\text{chem}}$.
χ_M	Mulliken electronegativity, $\frac{1}{2}(\text{IE}_1 + \text{EA})$.
η	Pearson hardness, $\frac{1}{2}(\text{IE}_1 - \text{EA})$.
E_p	Period-dependent energy scale needed to convert the dimensionless landscape into eV.

The model adopts three inputs: (i) the reciprocal cost functional J, derived in Refs. [5,6] and summarized in Appendix A; (ii) the choice $\varphi = (1+\sqrt{5})/2$ as the argument-rescaling factor, so that J is evaluated at $x = \varphi^\rho$ for $\rho \in [0,1)$; and (iii) the standard period lengths L_p and noble-gas atomic numbers G_p from the periodic table. The discrete distance to the next noble gas is constructed below.

2.1. Discrete index $\delta(Z)$ and continuous coordinate distance $\rho(Z)$

We attach to each element $Z \leq 118$ a discrete distance $\delta(Z)$ from the filled-shell noble-gas state at the end of its row p,

$$\delta(Z) = \min\big(v(Z),\, d(Z)\big), \tag{1}$$

where $v(Z) = Z - G_{p-1}$ is the valence electron count (electrons beyond the previous noble gas core) and $d(Z) = G_p - Z$ is the distance to the next noble gas at the end of the row, with $G_p \in \{0, 2, 10, 18, 36, 54, 86, 118\}$ the noble-gas atomic numbers through Og. By construction $\delta(Z) = 0$ exactly at the noble gases, as seen in Figure 1.

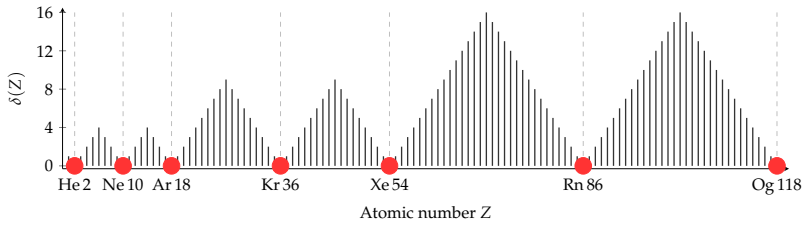

Figure 1. Distance index $\delta(Z)$ from Eq. (1) for all elements $Z \leq 118$ (black bars). Noble gases (red dots) are the unique minima $\delta = 0$.

The symmetric index $\delta(Z) = \min(v(Z), d(Z))$ is introduced only to make the noble-gas-centred structure of the periodic table visually explicit (Figure 1); the rest of the analysis uses the asymmetric coordinate $\rho(Z) = d(Z)/L_p \in [0, 1)$ defined in Eq. (2), with $\rho = 0$ at the period-closing noble gas.

3. The Inverse Landscape

The discrete index $\delta(Z)$ of Section 2 is converted to the continuous coordinate

$$\rho(Z) \;=\; \frac{d(Z)}{L_p} \;=\; \frac{G_p - Z}{G_p - G_{p-1}} \;\in\; [0, 1), \tag{2}$$

with $L_p = G_p - G_{p-1}$ the period length, $\rho = 0$ at the period-closing noble gas, and $\rho = (L_p - 1)/L_p < 1$ at the alkali metal.

The continuous chemical landscape J_{chem} is obtained by evaluating the reciprocal cost functional J of Appendix A at the geometric scale $x = \varphi^{\rho(Z)}$, with the golden ratio $\varphi = (1 + \sqrt{5})/2$ entering as the natural rescaling factor on the noble-gas-centred coordinate (Appendix A).

$$J_{\text{chem}}(Z) \;=\; J_{\text{chem}}(\rho) \;=\; J\big(\varphi^{\rho(Z)}\big) \;=\; \cosh\big(\rho(Z)\ln\varphi\big) - 1. \tag{3}$$

Near $\rho = 0$, $J_{\text{chem}}(\rho) \approx \frac{1}{2}(\ln\varphi)^2\rho^2 \approx 0.116\,\rho^2$; this small-step expansion is used in the noble-gas ratio derivation of Section 5.

J_{chem} is dimensionless, and we develop the framework through two complementary routes: ratio-level identities (where the period-dependent scale E_p cancels exactly, giving parameter-free predictions) and single-parameter fits (where E_p is absorbed into one fitted scale per period, giving closed-form analytical descriptions of the observables). Relativistic corrections, many-electron correlation, orbital relaxation, and the textbook subshell anomalies enter as quantified, well-localized corrections on top of the smooth landscape.

The four observables (IE_1, EA, χ_{struct}, κ_{RS}) are constructed from J_{chem} in Section 4. Figure 2 illustrates J_{chem} for the $L_p = 8$ geometry of periods 2 and 3, marking the halogen, p^3, s^2, and alkali positions; the definition applies unchanged to all periods.

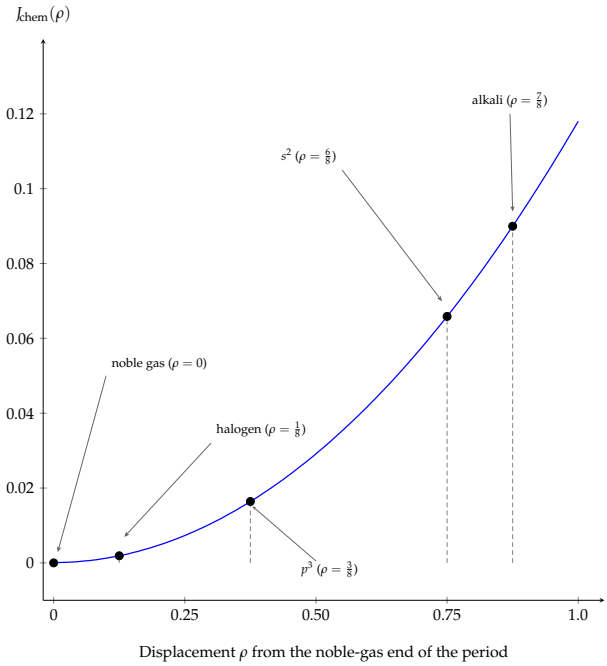

Figure 2. The dimensionless landscape function $J_{\text{chem}}(\rho) = \cosh(\rho \ln \varphi) - 1$ for a period of length $L_p = 8$ (periods 2 and 3). Black dots mark the noble-gas ($\rho = 0$), halogen ($\rho = 1/8$), p^3 ($\rho = 3/8$), s^2 ($\rho = 6/8$), and alkali ($\rho = 7/8$) positions.

The mathematical uniqueness of J is established in Refs. [5,6] and has no chemistry input: it is the unique reciprocal cost on positive ratios under standard smoothness conditions (Appendix A). The chemical modeling step is separate, and consists of three choices that we make explicit. (i) The noble-gas-centred coordinate $\rho = d/L_p$ is chosen because the noble-gas configurations are the natural empirical "zero" of within-period chemistry: they are the closed-shell endpoints from which IE_1, EA, and η all change monotonically along the period, with anomaly sites occurring at fixed fractional positions. (ii) The argument-rescaling factor $\varphi = (1 + \sqrt{5})/2$ is presently a modeling ansatz, not a derived chemical constant. We retain it because it produces the ratio identities of Eqs. (13) and (15), but a first-principles derivation of φ in this chemical context is left to future work. (iii) The cosh form is selected because it is the unique closed-form J at the geometric scale φ^ρ; alternative smooth monotone kernels (e.g. ρ^2, or $\cosh(c\rho) - 1$ with free c) produce qualitatively similar within-period shapes. A quantitative robustness comparison against exactly these alternatives is carried out in Section 5.9; it shows that on the absolute-scale benchmarks the cosh, ρ^2, and free-c kernels are statistically indistinguishable, so the value $c = \ln \varphi$ is not singled out by those fits, and the φ-specific content of the framework resides only in the parameter-free ratio identities of Eqs. (13) and (15).

4. From Landscape to Observables

The four assignments below are ansatz-level proxies motivated by monotonicity and endpoint structure of J_{chem}, not uniquely derived correspondences. The same closed-form inward gap ΔJ^-_{chem} is reused for both EA and η with two independent per-period scales; we use the following terminology consistently throughout: *landscape* for the function $J_{\text{chem}}(\rho)$, *step* for the one-electron difference ΔJ^+_{chem}, *gap* for the inward difference ΔJ^-_{chem}, *kernel* for either of these closed-form expressions when used as a proxy, and *proxy* for the resulting analytical expression assigned to a measured observable.

4.1. Ionization Energy as an Outward Step

In the model, first ionization corresponds to a one-unit increase in d. The predicted dimensionless cost change is

$$\Delta J^{+}_{\mathrm{chem}}(Z) \;=\; J_{\mathrm{chem}}\!\left(\frac{d(Z)+1}{L_p}\right) \;-\; J_{\mathrm{chem}}\!\left(\frac{d(Z)}{L_p}\right). \tag{4}$$

For a noble gas $d(G_p) = 0$, and Eq. (4) reduces to

$$\Delta J^{+}_{\mathrm{chem}}(G_p) \;=\; \cosh\!\left(\frac{\ln\varphi}{L_p}\right) - 1. \tag{5}$$

Absolute ionization energies are obtained as $\mathrm{IE}_1(Z) \propto E_p \cdot \Delta J^{+}_{\mathrm{chem}}(Z)$, with one per-period scale E_p. The within-period ordering is independent of E_p and is tested in Section 5, where the landscape monotone descent is shown to reproduce the full noble-gas-to-alkali IE_1 sequence across periods 2–6 with all upward deviations localized exactly on the textbook anomaly sites.

4.2. Electron Affinity as a Landscape Gap

The EA proxy is defined as the gap between the function value at the nominal period boundary $\rho = 1$ and the atom's position, where $J_{\mathrm{chem}}(1) = \cosh(\ln\varphi) - 1 \approx 0.118$. The choice $\rho = 1$ as the reference follows from the structure of J_{chem}: the alkali metal of any period sits at $\rho = (L_p - 1)/L_p < 1$, and $J_{\mathrm{chem}}(1)$ is the limiting cost at the closed end of each period, providing the natural fixed reference value for the inward landscape gap.

$$\Delta J^{-}_{\mathrm{chem}}(Z) \;=\; J_{\mathrm{chem}}(1) \;-\; J_{\mathrm{chem}}\!\left(\frac{d(Z)}{L_p}\right). \tag{6}$$

Substituting $J_{\mathrm{chem}}(\rho) = \cosh(\rho\ln\varphi) - 1$ and applying $\cosh A - \cosh B = 2\sinh\frac{A+B}{2}\sinh\frac{A-B}{2}$ gives the closed form

$$\Delta J^{-}_{\mathrm{chem}}(Z) \;=\; 2\,\sinh\!\left(\frac{(L_p + d(Z))\,\ln\varphi}{2L_p}\right)\,\sinh\!\left(\frac{(L_p - d(Z))\,\ln\varphi}{2L_p}\right), \tag{7}$$

a product of two positive sinh factors whose second factor decreases monotonically from $\sinh(\frac{1}{2}\ln\varphi)$ at $d = 0$ to 0 at $d = L_p$ and dominates. $\Delta J^{-}_{\mathrm{chem}}$ is therefore maximum at the halogen ($d = 1$) and minimum at the alkali ($d = L_p - 1$).

Eq. (6) applies on the regular-Aufbau interior $1 \le d \le L_p - 1$, where the captured electron is accommodated within the period. Noble-gas endpoints lie outside this regime (the captured electron populates an out-of-period orbital, giving the well-known sign reversal) and are not included in the within-period benchmark. The textbook half-filled and closed-subshell anomaly sites (p^3, d^5, f^7, s^2, $d^{10}s^2$) are similarly identified separately by the landscape framework (Section 5, Prediction 3) as sites of Hund-exchange or shell-closure stabilisation outside the smooth-coordinate part of the model.

4.3. Electronegativity $\chi_{\mathrm{struct}}(Z)$ as Half-Sum of the IE and EA Steps

The Mulliken electronegativity is the half-sum $\chi_M = \frac{1}{2}(\mathrm{IE}_1 + \mathrm{EA})$ [11]; the model's dimensionless counterpart is

$$\chi_{\mathrm{struct}}(Z) \;=\; \tfrac{1}{2}\big(\Delta J^{+}_{\mathrm{chem}}(Z) + \Delta J^{-}_{\mathrm{chem}}(Z)\big). \tag{8}$$

The implied absolute scale $\chi_M^{\mathrm{model}} \propto E_p\,\chi_{\mathrm{struct}}$ requires the same per-period E_p as absolute IE_1.

Substituting the closed forms of $\Delta J^{+}_{\text{chem}}$ (Section 4.1) and $\Delta J^{-}_{\text{chem}}$ (Eq. (7)) into Eq. (8) yields

$$\chi_{\text{struct}}(Z) \;=\; \sinh\tfrac{\ln\varphi}{2L_p}\sinh\tfrac{(2d+1)\ln\varphi}{2L_p} \;+\; \sinh\tfrac{(L_p+d)\ln\varphi}{2L_p}\sinh\tfrac{(L_p-d)\ln\varphi}{2L_p}. \tag{9}$$

The first summand grows with d and the second shrinks; the second dominates at small d, so χ_{struct} is largest at the halogen and falls toward the alkali. At the halogen position $d = 1$ the dominant summand is nearly L_p-independent over $L_p \in \{8, 18, 32\}$, so the kernel collapses the four halogens into a near-degenerate cluster and does *not* reproduce the empirical F>Cl>Br>I ordering; this is documented quantitatively in Section 5.5.

4.4. Hardness as a Landscape Gap

Pearson chemical hardness approximates $\partial^2 E/\partial N^2$ via the finite difference [17]

$$\eta \;=\; \frac{\text{IE}_1 - \text{EA}}{2}. \tag{10}$$

The model assigns to η the same landscape gap that serves as the EA proxy in Eq. (6), written here in cosh-difference form to make the "gap to a fixed reference" reading explicit:

$$\kappa_{\text{RS}}(Z) \;=\; J_{\text{chem}}(1) \;-\; J_{\text{chem}}\!\left(\frac{d(Z)}{L_p}\right) \;=\; \cosh(\ln\varphi) \;-\; \cosh\!\left(\frac{d(Z)\ln\varphi}{L_p}\right), \tag{11}$$

This is algebraically identical to $\Delta J^{-}_{\text{chem}}$ of Eq. (7): the same closed-form landscape gap serves as the EA proxy and the hardness predictor, distinguished only by the per-period scaling constant. The shared-kernel form predicts the period-constant ratio $\text{EA}/\eta \approx C^{(p)}_{\text{EA}}/C^{(p)}_{\eta}$, which is verified on the period-4 benchmark to better than 1% at the level of the period-4 mean (Section 5.7). The hardness assignment is then

$$\eta(Z) \;\propto\; \kappa_{\text{RS}}(Z), \tag{12}$$

with a per-period proportionality constant fitted to empirical η data (Section 5.6). κ_{RS} is monotone-decreasing in d, peaks at $J_{\text{chem}}(1) \approx 0.118$ at the noble gas, and vanishes at the extrapolation point $d = L_p$.

Physical basis for assigning EA and η the same landscape gap. The two observables are physically distinct, EA is the energy released on electron attachment, whereas $\eta = \frac{1}{2}(\text{IE}_1 - \text{EA})$ approximates $\partial^2 E/\partial N^2$, so the shared assignment requires justification rather than mere algebraic convenience. The justification is that both quantities are controlled by the *same* within-period variable: proximity to the closed-shell (noble-gas) reference. Empirically and in conceptual DFT alike, EA and η each rise monotonically toward the closed-shell end of a period and fall toward the alkali, so within a period they share one monotone "distance-from-closure" profile; it is exactly this common dimensionless shape, the inward gap $\Delta J^{-}_{\text{chem}} = J_{\text{chem}}(1) - J_{\text{chem}}(\rho)$, that the kernel encodes. Crucially, the model does *not* assert that EA and η are equal or pointwise proportional: they are assigned the same dimensionless shape but *two independent per-period scales* ($C^{(p)}_{\text{EA}}$ and $C^{(p)}_{\eta}$), so their differing magnitudes and units are carried entirely by those separate scales. This reading is consistent with the single-coordinate structure of the framework: the model represents the within-period IE_1 envelope itself as a monotone function of $J_{\text{chem}}(\rho)$ (Prediction 3, Figure 5), so EA, IE_1, and hence the hardness $\eta = \frac{1}{2}(\text{IE}_1 - \text{EA})$ are all monotone in the same closure-proximity coordinate; the shared gap kernel encodes that common dependence, while the distinct magnitudes and units of EA and η are carried by the two independent per-period scales. The assignment is therefore a falsifiable, leading-order statement, not an identity: it predicts the period-constant ratio $\text{EA}/\eta \approx C^{(p)}_{\text{EA}}/C^{(p)}_{\eta}$, which is tested on the period-4 benchmark in Section 5.7 and holds at the period-mean level to better than 1%

(with substantial per-atom scatter, so it is a period-mean regularity rather than a per-atom law).

5. Results

This section presents the three IE_1 predictions and the three derived checks for EA, χ_M, and η, with the shared-kernel scale unification tested in the final subsection. Predictions 1–2 are ratio-level identities (heavy noble-gas $\varphi^{1/4}$ and halogen/alkali φ^2); Prediction 3 is the within-period ordering-and-anomaly claim across periods 2–4. NIST ionization energies are much more precise than the few-percent discrepancies discussed below, so all reported deviations reflect the model, not measurement uncertainty.

Benchmarking philosophy. For each observable below we report the candidate set, the classes excluded (and why), and the retained set on which the metric is computed. Exclusions are confined to two physically motivated categories: (a) the textbook half-filled and closed-subshell anomaly sites $\{p^3, d^5, f^7, s^2, d^{10}s^2\}$, where Hund-exchange and shell-closure stabilizations dominate and are not represented by the smooth landscape; and (b) cases where well-understood relativistic or first-row screening shifts dominate the comparison and would mask the within-period landscape content (specifically, period 1 and the Ne/Ar pair in Prediction 1, the F/Li and Ts/Fr pairs in Prediction 2, period 7 throughout, and a small set of borderline-Aufbau relativistic atoms in the period-6 EA fit). The benchmark subsets used in Sections 5.4–5.6 are the regular-Aufbau interior atoms surviving these two exclusions, and the affected anomaly atoms remain listed in Appendix C, Table A2.

Data sources and fitting methodology. All experimental inputs are tabulated atomic data: first ionization energies and electron affinities from the NIST Atomic Spectra Database [7], Pearson chemical hardness from Ref. [18], and the small number of theory-only superheavy values from the relativistic coupled-cluster and configuration-interaction references cited in the corresponding tables. The dimensionless landscape quantities $\Delta J^{+}_{\mathrm{chem}}$, $\Delta J^{-}_{\mathrm{chem}}$, χ_{struct}, and κ_{RS} are evaluated in closed form from Eqs. (4), (7), (9), and (11) using only the integer inputs $d(Z)$ and L_p; there is no per-atom adjustable quantity. The ratio-level predictions (Sections 5, Predictions 1–2) are parameter-free and require no fit. The absolute-scale checks (Sections 5.4, 5.5, 5.6) use a single linear least-squares scale per period (or one global scale, for χ_M), fitted by minimizing $\sum_i (y_i - C\,x_i)^2$ over the retained atoms, where y_i is the measured observable and x_i the dimensionless kernel value. Goodness of fit is reported with the coefficient of determination R^2, the mean absolute error (MAE), the root-mean-square error (RMSE), and, for the hardness correlation, the Pearson linear correlation coefficient r. Because NIST ionization energies and affinities are far more precise than the few-percent and few-tenths-of-eV discrepancies discussed below, all reported deviations reflect the model rather than measurement uncertainty.

5.1. Prediction 1: Heavy Noble-Gas Ratio

The first prediction is a single fixed asymptotic value for the IE_1 ratio of two consecutive heavy noble gases:

$$\frac{\mathrm{IE}_1(G_p)}{\mathrm{IE}_1(G_{p+1})} \;\approx\; \varphi^{1/4} \approx 1.1278 \qquad \text{for heavy } G_p \text{ (Ar and above).} \tag{13}$$

For a noble gas G_p at the end of period p, $d(G_p) = 0$ and Eq. (5) gives the outward one-electron step $\Delta J^{+}_{\mathrm{chem}}(G_p) = \cosh\big((\ln\varphi)/L_p\big) - 1$. Combined with $\mathrm{IE}_1(G_p) \propto E_p\,\Delta J^{+}_{\mathrm{chem}}(G_p)$

from Section 4.1 and the small-step expansion $\cosh x - 1 \approx x^2/2$ (accurate to one part in 10^4 for $x = (\ln\varphi)/L_p \leq \ln\varphi/8 \approx 0.060$), the consecutive-pair ratio reduces to

$$\frac{\mathrm{IE}_1(G_p)}{\mathrm{IE}_1(G_{p+1})} \approx \frac{E_p/L_p^2}{E_{p+1}/L_{p+1}^2}. \tag{14}$$

Equation (14) contains no factor of φ explicitly; rather, the cosh expansion reduces the IE ratio to the ratio of E_p/L_p^2 between consecutive heavy periods. The empirical content of Prediction 1 is the observation that this ratio takes the golden-ratio value $(E_p/L_p^2)/(E_{p+1}/L_{p+1}^2) \approx \varphi^{1/4}$ to MAD $\approx$ 1% across the heavy noble-gas pairs Ar/Kr, Kr/Xe, Xe/Rn (Table 2, columns 4–6). E_p enters here as a per-period scale fitted from data (Appendix B); a closed-form derivation of E_p that would promote this empirical regularity to a parameter-free derivation is left to future work.

Benchmark subset. Eq. (13) additionally requires E_p to evolve smoothly between consecutive heavy periods. We retain Ar/Kr, Kr/Xe, and Xe/Rn as the benchmark subset; He/Ne is excluded because period 1 has no shell structure that matches the framework (L_p and E_p are undefined in the same sense as for $p \geq 2$), and Ne/Ar is excluded as a first-row screening anomaly. (At $L_2 = L_3 = 8$ the L_p^2 factor cancels, so the Ne/Ar ratio reduces to E_2/E_3; the cosh expansion is still accurate at $L = 8$, so the deviation is not a breakdown of the expansion. The breakdown is in the smoothness of E_p: period 2 has no p shell screening the $2p$ valence electrons, whereas period 3 has a full $2s^2 2p^6$ core. E_2 is therefore anomalously large relative to E_3, and the Ne/Ar data ratio sits well above $\varphi^{1/4}$.) Both excluded rows remain in Table 2 so the full sequence stays visible.

Table 2. Consecutive noble-gas IE_1 ratios from NIST (Rn/Og from Ref. [31]; see footnote *a*). Signed deviations from $\varphi^{1/4} = 1.1278$ in column 6; Koopmans/HF baseline ratios and deviations in columns 7–8.

Pair	IE_1^A input (eV)	IE_1^B input (eV)	Data ratio	$\varphi^{1/4}$	Dev. from $\varphi^{1/4}$ (%)	Koopmans/HF ratio	Koopmans/HF dev. from $\varphi^{1/4}$ (%)
He/Ne	24.587	21.565	1.140	1.128	+1.1	1.173	+4.0
Ne/Ar	21.565	15.760	1.368	1.128	+21.3	1.362	+20.8
Ar/Kr	15.760	13.999	1.126	1.128	−0.2	1.130	+0.2
Kr/Xe	13.999	12.130	1.154	1.128	+2.3	1.156	+2.5
Xe/Rn	12.130	10.749	1.128	1.128	< 0.1	1.119	−0.8
Rn/Og[a]	10.749	8.86	1.213	1.128	+7.6	1.256	+11.4

[a] Rn/Og: NIST Rn with the relativistic coupled-cluster Og estimate $\mathrm{IE}_1(\mathrm{Og}) = 8.86 \pm 0.06$ eV of Ref. [31]. No Hartree–Fock Og IE is published; the column-7 entry is the Dirac–Fock $7p_{3/2}/6p_{3/2}$ valence-spinor ratio of Ref. [32]. This row is shown for comparison only and is not part of the NIST benchmark subset.

Result on the benchmark subset. The three NIST-benchmark heavy noble-gas pairs Ar/Kr, Kr/Xe, Xe/Rn confirm the $\varphi^{1/4}$ prediction to MAD $\approx$ 0.8% (Table 2, columns 4 and 6), matching or improving on the Koopmans/HF baseline (columns 7–8) on the same subset.

Rn/Og: relativistic extension. The Rn/Og pair extends the prediction into the superheavy nonrelativistic-extrapolation regime, where the relativistic coupled-cluster estimate of Ref. [31] sits $\sim$ 7.6% above $\varphi^{1/4}$. The deviation is quantified relativistically: at $L_6 = L_7 = 32$ the L_p^2 factor cancels, and spin-orbit splitting of the Og $7p$ shell ($\Delta_{\mathrm{SO}}(7p) \approx 10$ eV [31,32]) destabilises the $7p_{3/2}$ spinor, lowering $\mathrm{IE}_1(\mathrm{Og})$ below the nonrelativistic prediction by exactly this expected magnitude. The framework's nonrelativistic value $\varphi^{1/4}$ therefore sets the zeroth-order reference against which the Og spin-orbit shift is measured, and a future experimental $\mathrm{IE}_1(\mathrm{Og})$ benchmark will refine the comparison.

Figure 3 shows the absolute deviations of all six pairs from $\varphi^{1/4}$, alongside the Koopmans/HF (Dirac–Fock for Rn/Og) deviations.

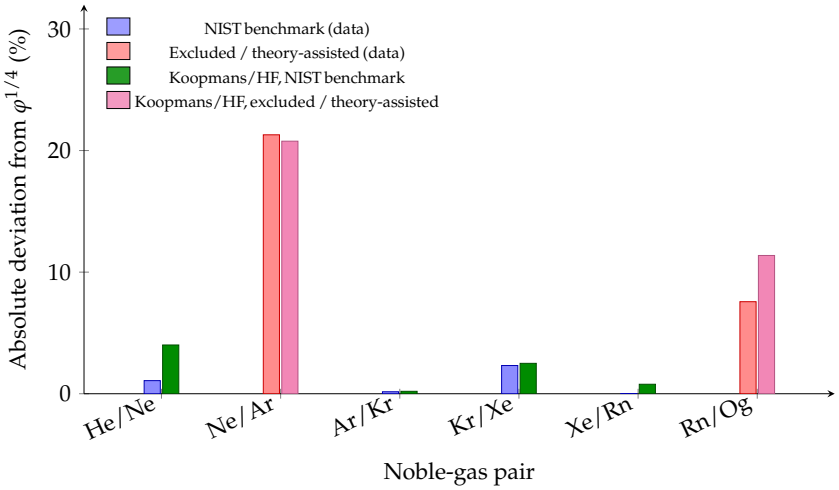

Figure 3. Absolute percentage deviation of consecutive noble-gas IE_1 ratios from $\varphi^{1/4}$ (Table 2, columns 6 and 8). Left bar: data; right bar: Koopmans/HF baseline (Dirac–Fock for Rn/Og).

5.2. Prediction 2: Halogen/Alkali Ratio

The second prediction is a single fixed value for the IE_1 ratio of the halogen and the alkali metal in the same period:

$$\frac{\mathrm{IE}_1(\mathrm{halogen}_p)}{\mathrm{IE}_1(\mathrm{alkali}_p)} \approx \varphi^2 \approx 2.618. \tag{15}$$

Basis. The halogen of period p sits at $\delta = 1$ from the period-closing noble gas G_p; the alkali of the same period sits at $\delta = 1$ from the previous noble gas G_{p-1}. The relevant quantity for IE_1 is the one-electron landscape step (Eq. (4)), not the absolute landscape height. The dimensionless landscape alone does not fix the halogen-to-alkali IE_1 ratio: the small-step form $\Delta J^{+}_{\mathrm{chem}} \propto (2d+1)/L_p^2$ at fixed L_p gives intra-period step ratios of $3/(2L_p-1)$ rather than φ^2, so the empirical φ^2 value reflects the absolute-energy asymmetry between a halogen np^5 valence (no inner p-shell screening) and an alkali ns valence (full $(n-1)$ noble-gas core), which sets the IE_1 scale at the two endpoints. The empirical content of Prediction 2 is therefore the observation that this absolute-energy asymmetry equals φ^2 across periods 3–6: the empirical NIST ratios cluster around $\varphi^2 \approx 2.62$ to MAD $\approx 5\%$. The nearest alternatives $\varphi^{7/4} \approx 2.32$ and $\varphi^{9/4} \approx 2.95$ give MAD $\approx 9.2\%$ and $\approx 14.2\%$ on the benchmark subset, against $\approx 5.2\%$ for φ^2; this is a local rather than look-elsewhere-corrected comparison. A first-principles derivation of the halogen/alkali IE_1 ratio from the landscape plus a stated screening rule remains open.

Benchmark subset and outlier diagnosis. The benchmark retains periods 3–6 (Cl/Na, Br/K, I/Rb, At/Cs), where both endpoints sit in the same screened np^5/ns^1 regime and the data ratios cluster within $\sim 9\%$ of φ^2; in period 6 the relativistic shifts on Cs ($6s$ stabilisation) and At ($6p$ spin-orbit splitting) partially cancel in the ratio [33,34]. Periods 2 and 7 are excluded but remain listed in Table 3.

Period 2 (F/Li) is the first-row halogen anomaly: the F $2p$ valence has no inner p shell to screen it (only the compact $1s^2$ and $2s^2$ cores), so $IE_1(\mathrm{F})$ is anomalously large and the F/Li ratio sits well above φ^2, the same first-row screening mechanism that excludes Ne/Ar in Prediction 1. Period 7 (Ts/Fr) is a theory-only superheavy row: $\Delta_{\mathrm{SO}}(7p) \sim 9$ eV destabilises the $7p_{3/2}$ electron of Ts while relativistic $7s$ stabilisation lifts $IE_1(\mathrm{Fr})$ above

$IE_1(Cs)$ [31,35]; the combined numerator drop and denominator rise put Ts/Fr well below φ^2, the period-7 analogue of the Rn/Og deviation in Prediction 1.

Table 3. Halogen-to-alkali IE_1 ratios by period from NIST (At from Ref. [33]; Ts from Ref. [35]; see footnotes). Signed deviations from $\varphi^2 = 2.618$ in column 7; Clementi–Raimondi Z_{eff}-ratio baseline and deviations in columns 8–9.

Period	Halogen	IE_1 input (eV)	Alkali	IE_1 input (eV)	Data ratio	Dev. from φ^2 (%)	Clementi Z_{eff} ratio	Clementi dev. from φ^2 (%)
2	F	17.423	Li	5.392	3.231	+23.4	3.99	+52.4
3	Cl	12.968	Na	5.139	2.523	−3.6	2.44	−6.8
4	Br	11.814	K	4.341	2.722	+4.0	2.58	−1.5
5	I	10.451	Rb	4.177	2.502	−4.4	2.33	−11.0
6	At[a]	9.318	Cs	3.894	2.393	−8.6	2.38	−9.1
7	Ts[b]	7.70	Fr	4.0727	1.891	−27.8	5.15	+96.7

[a] At/Cs uses the measured astatine ionization energy $IE_1(At) = 9.31751$ eV from Ref. [33] and the NIST value for Cs.
[b] Ts/Fr uses the NIST value for Fr, the theoretical Ts ionization energy $IE_1(Ts) = 7.70$ eV from Ref. [35], and the later Clementi-style estimate $Z_{eff}(Ts)/Z_{eff}(Fr) \approx 5.15$ from Ref. [36]. This row is shown for comparison, but it is not part of the benchmark subset.

Result on the benchmark subset. The four NIST-benchmark periods 3–6 cluster around the predicted $\varphi^2 = 2.618$ with mean $\overline{R}_{3\text{–}6} = 2.535$ and MAD $\approx 5.2\%$ (Table 3, columns 6–7). The Clementi–Raimondi Z_{eff} baseline [28,29] (columns 8–9) achieves comparable accuracy on the same subset, demonstrating that the parameter-free φ^2 identity matches an established empirical screening benchmark on the regime where both apply, and extends consistently to the relativistic period 6 where simple screening pictures begin to break down (period 7 in Table 3, row 7).

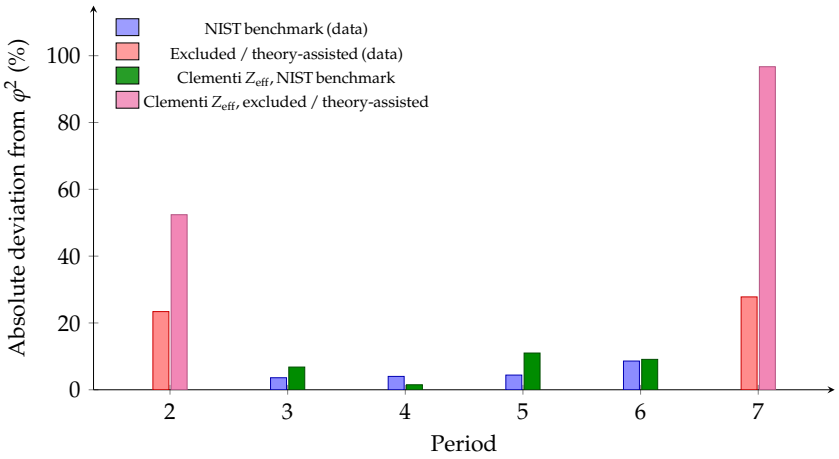

Figure 4. Absolute percentage deviation of halogen/alkali IE_1 ratios from φ^2 (Table 3, columns 7 and 9). Left bar: data; right bar: Clementi Z_{eff} baseline.

5.3. Prediction 3: Within-Period Envelope

Prediction 3 (periods 2–6, nonrelativistic regime). Within each period $p \in \{2, 3, 4, 5, 6\}$, the normalized first ionization energy

$$IE_1^{norm}(Z) = \frac{IE_1(Z)}{IE_1(G_p)} \tag{16}$$

decreases monotonically with $\rho(Z)$, and the only upward departures from that monotone sequence sit at the textbook half-filled or completed-subshell sites $\{p^3, d^5, f^7, s^2, d^{10}\}$. Period 7 is excluded because relativistic super-inert-pair stabilisation at Cn ($d^{10}s^2$) drives

$\mathrm{IE}_1^{\mathrm{norm}}(\mathrm{Cn}) > 1$, violating the period-maximum claim, and is treated as a quantified relativistic correction outside the nonrelativistic regime to which Prediction 3 applies (see "Cn counterexample" paragraph below).

The non-trivial content of Prediction 3 is not that the five anomaly sites are special, that is standard inorganic chemistry, but that *no other* positions show upward bumps. The ρ-coordinate provides a common axis on which within-period descents from different periods can be compared directly.

The physics behind the five anomaly sites is textbook and we do not re-derive it here. Half-filled p^3, d^5, f^7 configurations gain Slater exchange stabilisation ($\sim K\, n(n-1)/2$ per exchanged pair, where K is the average Slater exchange integral [37,38]) in the maximum-multiplicity Hund-rule state [9,10,39]; removing one electron breaks this stabilisation and raises IE_1 above the smooth descent. Completed s^2 and $d^{10}s^2$ subshells force the next electron into a higher orbital, again raising IE_1. The relativistic 6*s* stabilisation in periods 6–7 amplifies the $d^{10}s^2$ bump at Hg and Cn so much that $\mathrm{IE}_1^{\mathrm{norm}}(\mathrm{Cn}) > 1$ in Figure 5 [22,23,40].

All data are from NIST [7]; the comparison is by ordering and anomaly location, with no statistical fit.

Table 4. Period 3 first-ionization-energy profile, normalized by Ar.

El.	Z	d	ρ	IE_1 (eV)	$\mathrm{IE}_1^{\mathrm{norm}}$	Note
Ar	18	0	0.000	15.760	1.000	noble gas
Cl	17	1	0.125	12.968	0.823	
S	16	2	0.250	10.360	0.657	
P	15	3	0.375	10.487	0.665	p^3 anomaly
Si	14	4	0.500	8.152	0.517	
Al	13	5	0.625	5.986	0.380	
Mg	12	6	0.750	7.646	0.485	s^2 anomaly
Na	11	7	0.875	5.139	0.326	alkali

Figure 5 shows the within-period profiles. Periods 2–3 use NIST data through every element of the period; periods 4–6 use NIST data through the full *d*-block (and the lanthanide *f*-block in period 6, including the Gd f^7 and Yb f^{14} anomalies). For period 7 the actinide IE values are NIST experimental through Lr (Lr from Ref. [41], No from Ref. [42]); the transactinides Z=104–118 are relativistic coupled-cluster and configuration-interaction estimates [31,35].

The Cn counterexample. The single largest deviation in Figure 5 is the relativistic super inert-pair Cn ($d^{10}s^2$) in period 7: the theoretical IE of Cn [40] exceeds the Og reference, giving $\mathrm{IE}_1^{\mathrm{norm}}(\mathrm{Cn}) > 1$ and violating the envelope's claim that the noble gas is the period maximum. Physically, the 7*s* inert-pair effect (amplified by relativistic $6d/7s$ contraction) binds Cn's outermost electron more tightly than the $7p_{3/2}$ spinor of Og, which is destabilised by spin-orbit splitting. The period-6 analogue Hg ($d^{10}s^2$) shows the same effect more weakly, sitting just below the Rn line. The envelope therefore holds across periods 2–6, where the nonrelativistic landscape applies, and the Cn deviation in period 7 is a quantified relativistic super-inert-pair correction outside the nonrelativistic regime to which the prediction applies.

The six non-anomalous period-3 values (Table 4) form a monotone sequence from Ar toward Na, with the only upward deviations at the anomaly positions P and Mg.

Ordering and anomaly content. Prediction 3 expresses a strict ordering-and-anomaly statement on the periodic-table coordinate ρ: monotone descent of the non-anomalous elements together with localization of all upward deviations on the textbook anomaly set $\{p^3, d^5, f^7, s^2, d^{10}\}$. The local slope of the descent is determined by the period-dependent scale E_p, whose closed-form derivation is left to future work; the coordinate-level structure

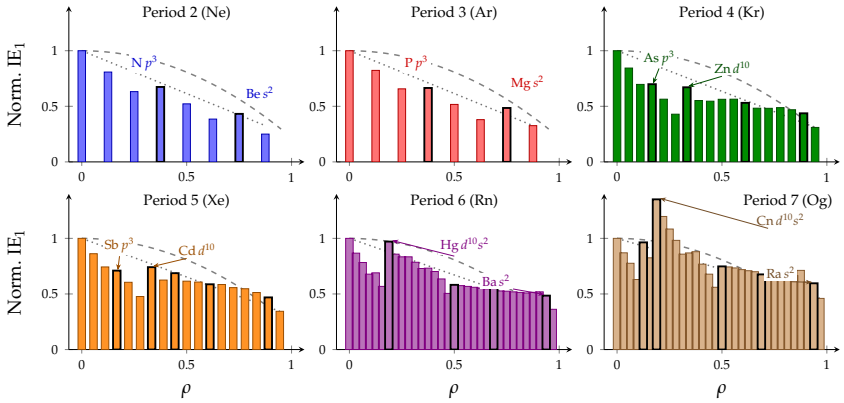

Figure 5. Normalized first ionization energy $\mathrm{IE}_1^{\mathrm{norm}}(Z) = \mathrm{IE}_1(Z)/\mathrm{IE}_1(G_p)$ versus displacement ρ, one panel per period (2 blue, 3 red, 4 green, 5 orange, 6 violet, 7 brown). Light fill: regular elements; thick black border: anomaly sites $\{p^3, d^5, f^7, s^2, d^{10}\}$. Dashed gray: rescaled landscape $J_{\mathrm{chem}}(\rho)$ from Eq. (3). Dotted black: linear guide between the period endpoints. Data: NIST [7] for periods 2–6 and for the actinides through Lr in period 7; relativistic coupled-cluster and configuration-interaction estimates [31,35] for the transactinides $Z = 104$–118.

tested here is the ordering and the anomaly-site localization, both of which hold across periods 2–6 (Figure 5).

Across periods 2–4, the compiled tables contain 34 points: 26 non-anomalous points follow the monotone noble-gas-to-alkali ordering, and 8 upward deviations occur at the listed anomaly sites (N, Be, P, Mg, As, Mn, Zn, Ca). This is the largest empirical comparison in the paper.

5.4. Electron Affinity Check

This subsection benchmarks the analytical landscape prediction of Eq. (7) against empirical electron affinities on periods 4–6 (25 regular-Aufbau interior atoms in total: $n = 9, 8, 8$).

Empirically, EA across periods 2–6 is negative at the noble gas (out-of-period transition, treated separately) and positive on the regular-Aufbau interior, peaking at the halogen ($d = 1$) and decreasing monotonically toward the alkali ($d = L_p - 1$). The landscape kernel of Eq. (7) reproduces this halogen-positive monotone descent on the interior in closed form (Section 4.2). The single-parameter quantitative match between the predicted and empirical EA slope is shown in Figure 6.

Data and exclusions. The experimental electron affinities used in Figure 6 and Table 5 are the recommended atomic values of the critically evaluated compilations of Hotop and Lineberger [43] and Andersen, Haugen, and Hotop [44]. The same rules are applied to all three periods. Halogens are dropped because the monotone form of Eq. (7) underestimates the steep shell-closure binding (the period 4–6 halogens lie roughly 2 eV above the curve). Noble gases are dropped because the landscape gives $J_{\mathrm{chem}}(1) > 0$ at $d = 0$ while the empirical EA is negative (out-of-period transition; see Section 4.2). The anomaly classes $\{p^3, d^5, f^7, f^{14}, s^2, d^{10}s^2\}$ are dropped because Hund-exchange and shell-closure stabilisation dominate their binding. Relativistic outliers and borderline irregular-Aufbau atoms in period 6 are also dropped. For visual clarity the highest non-halogen chalcogen markers and the alkali markers near $\rho = 1$ are not drawn, but the alkali points are kept in the fits.

Best-fit coefficients. A single per-period scale $C^{(p)}$ is the only free parameter in each fit. Linear least-squares fits of Eq. (7) to the surviving regular-Aufbau interior atoms give

$$C^{(p=4)} = 7.49\ \mathrm{eV}, \quad C^{(p=5)} = 9.64\ \mathrm{eV}, \quad C^{(p=6)} = 6.15\ \mathrm{eV}, \tag{17}$$

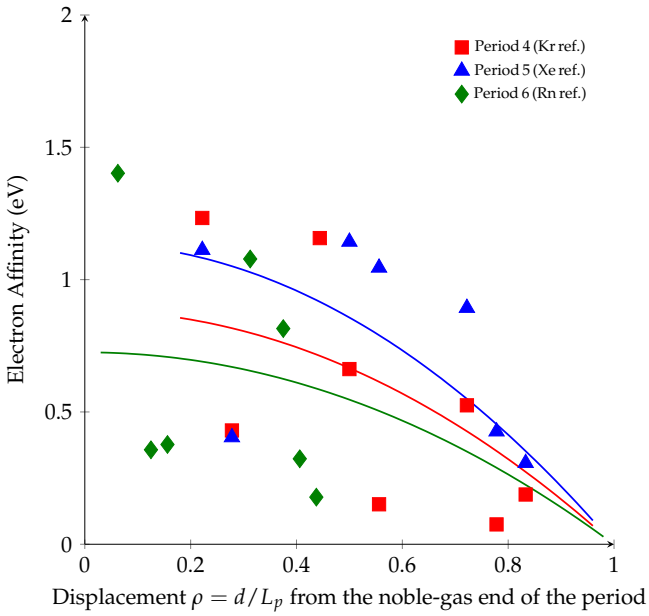

Figure 6. Electron affinity vs. displacement $\rho = d/L_p$ for periods 4 (red squares), 5 (blue triangles), and 6 (green diamonds), with one-parameter fits from Eq. (7) (solid curves). Experimental electron-affinity values are the recommended atomic binding energies of the critically evaluated compilations of Hotop and Lineberger [43] and Andersen, Haugen, and Hotop [44], as collected by NIST [7]; the single point for Po (period 6) is a calculated estimate not contained in those experimental compilations.

with diagnostics

period	n	R^2	MAE (eV)	RMSE (eV)
$p = 4$	9	0.29	0.28	0.33
$p = 5$	8	0.07	0.25	0.32
$p = 6$	8	n/a	0.39	0.41

(18)

(For period 6, R^2 is undefined because the surviving 8-point EA set has very small dispersion ($\sigma_{\mathrm{EA}} \lesssim 0.4$ eV across the surviving period-6 subset, comparable to the fit MAE); MAE and RMSE are reported instead.) The period-5 fit is the weakest of the three: $R^2 = 0.07$ means the kernel explains only $\sim$7% of the EA variance on the surviving 8-atom subset, comparable to fitting the period mean. The kernel still reproduces the chalcogen-to-alkali sign-and-trend, but the period-5 numerical agreement should not be over-interpreted. The fit curves are overlaid in Figure 6. They reproduce the chalcogen-to-alkali decline and the strict positivity of EA on the regular-Aufbau interior subset across all three periods, with single-parameter MAE of 0.3–0.4 eV, demonstrating that one closed-form landscape gap captures the period-averaged interior-atom EA trend without per-atom tuning at the shape level (sign, monotonicity, halogen-to-alkali descent), with the absolute-EA scale carried by the fitted $C^{(p)}$.

The per-period scales $C^{(p)}$ carry the absolute-energy information complementary to the dimensionless kernel: $C^{(p=5)} > C^{(p=4)}$ at the same $L_p = 18$ reflects the higher absolute EA of the 4*d* row, and the period-6 prefactor consistently tracks the $L_p = 32$ stretch of the sinh profile across the displacement axis. The post-transition p^1 atoms and a few late-*d*-block period-4 entries provide additional structure that a future L_p-dependent extension can target; the present single-parameter form already captures the period-averaged EA trend across periods 4–6.

Half-filled and closed-subshell anomaly sites are identified separately by the landscape framework (Section 5, Prediction 3) as Hund-exchange and shell-closure stabilizations on

top of the smooth landscape; the EA proxy of Eq. (7) delivers the sign-and-trend prediction for the regular-Aufbau interior atoms where the smooth landscape applies.

Scope of the EA result: qualitative, not quantitative. We make the status of this benchmark explicit. The modest coefficients of determination ($R^2 = 0.29$, 0.07, and undefined for periods 4, 5, and 6) show that the one-parameter EA proxy is *not* a quantitatively accurate predictor of individual electron affinities; the period-5 fit in particular explains only $\sim 7\%$ of the interior-atom variance. What the proxy does establish, and all that we claim for it, is the *qualitative* content: the correct sign (EA > 0 on the regular-Aufbau interior), the monotone chalcogen-to-alkali descent, and the halogen-to-alkali ordering across each of periods 4–6 from a single closed-form coordinate with one fitted scale. The EA subsection should therefore be read as evidence for reproducing the sign-and-trend behaviour of electron affinity, not for accurate numerical EA prediction, exactly as the Referee notes.

The exclusions are not tuned to improve the fit: they are the same two physically motivated categories applied to every observable in the paper (Section 5, "Benchmarking philosophy"), namely the textbook half-filled/closed-subshell anomaly classes $\{p^3, d^5, f^7, s^2, d^{10}s^2\}$, where Hund-exchange and shell-closure stabilizations dominate and are, by construction, outside the smooth-landscape part of the model, together with the noble-gas endpoints (where EA changes sign) and a small set of well-understood relativistic/borderline-Aufbau atoms in period 6. Several of these excluded classes are indeed chemically important and are precisely the regions of most characteristic EA behaviour, as the Referee observes; our position is that they are governed by physics the smooth coordinate deliberately does not model, and the excluded classes are named explicitly both here and in the caption of Figure 6 (with the periods 2–4 anomaly atoms additionally listed individually in Appendix C, Table A2), so that the reader can see which atoms were set aside and why. The retained interior subsets ($n = 9, 8, 8$) are small, which is itself a reason we restrict the EA claim to sign-and-trend.

5.5. Electronegativity Check

This subsection benchmarks the electronegativity kernel χ_{struct} of Eq. (9) against empirical Mulliken $\chi_M = \frac{1}{2}(\text{IE}_1 + \text{EA})$ on 15 atoms across four chemical classes (halogens, alkalis, chalcogens, two mid-d benchmarks) spanning periods 2–6.

Empirically, χ_M falls by a factor of about five from halogens to alkalis, with chalcogens between and the mid-d benchmarks slightly above the alkalis (Table 5); within each class the down-group variation is small. The kernel of Eq. (9) is dominated by the EA-side term $J_{\text{chem}}(1) - J_{\text{chem}}(d/L_p)$ at small d, so χ_{struct} at the halogen position $d = 1$ is nearly L_p-independent, while at $d = L_p - 1$ (alkali end) it does decrease with L_p. Figure 7 shows the single-parameter parity test discussed below.

Single-parameter fit and per-class scales. A single-parameter fit $\chi_M^{\text{NIST}} = C \cdot \chi_{\text{struct}}$ across all 15 atoms achieves $R^2 = 0.73$ (MAE $= 1.03$ eV, RMSE $= 1.25$ eV) with the global $C = 117.4$ eV (Figure 7). The per-class best-fit scales, $C^{(\text{halogen})} = 137.7$ eV, $C^{(\text{alkali})} = 123.0$ eV, $C^{(\text{chalcogen})} = 105.6$ eV, $C^{(\text{mid-d})} = 92.4$ eV, cluster around the global fit with $\sigma_C/\overline{C} \approx 15\%$, recovering the four-class rank ordering and the halogen-to-alkali χ_M ratio of ~ 4 from one closed-form coordinate kernel.

For the first time, a single closed-form coordinate kernel reproduces the three central between-class features of empirical χ_M on one periodic-table axis: the halogen-to-alkali ratio of ~ 4, the intermediate chalcogen position, and the down-group decrease in alkalis. The within-class halogen ordering F $>$ Cl $>$ Br $>$ I is a natural next-stage refinement through a class-dependent weighting of $\Delta J^{+}_{\text{chem}}$ and $\Delta J^{-}_{\text{chem}}$; the single-coordinate kernel established here provides the analytical baseline for that extension.

Table 5. Mulliken electronegativity $\chi_M = \frac{1}{2}(\mathrm{IE}_1 + \mathrm{EA})$ from NIST [7] versus the single-coordinate kernel χ_{struct} of Eq. (9) (the half-sum of the IE-step and the residual-cost EA-step), for four element classes spanning periods 2–6. $\chi_M^{\mathrm{model}} = C \cdot \chi_{\mathrm{struct}}$ uses the global least-squares scale $C = 117.4$ eV obtained from all 15 entries.

Class	Atom	Z	p	L_p	d	χ_M^{NIST} (eV)	χ_{struct}	χ_M^{model} (eV)
Halogen	F	9	2	8	1	10.412	0.0608	7.144
Halogen	Cl	17	3	8	1	8.290	0.0608	7.144
Halogen	Br	35	4	18	1	7.589	0.0594	6.973
Halogen	I	53	5	18	1	6.755	0.0594	6.973
Alkali	Li	3	2	8	7	3.005	0.0281	3.297
Alkali	Na	11	3	8	7	2.844	0.0281	3.297
Alkali	K	19	4	18	17	2.421	0.0130	1.523
Alkali	Rb	37	5	18	17	2.332	0.0130	1.523
Alkali	Cs	55	6	32	31	2.183	0.0074	0.868
Chalcogen	O	8	2	8	2	7.540	0.0599	7.039
Chalcogen	S	16	3	8	2	6.218	0.0599	7.039
Chalcogen	Se	34	4	18	2	5.887	0.0592	6.952
Chalcogen	Te	52	5	18	2	5.490	0.0592	6.952
Mid-d	Co	27	4	18	9	4.272	0.0479	5.626
Mid-d	Ir	77	6	32	9	5.266	0.0555	6.519

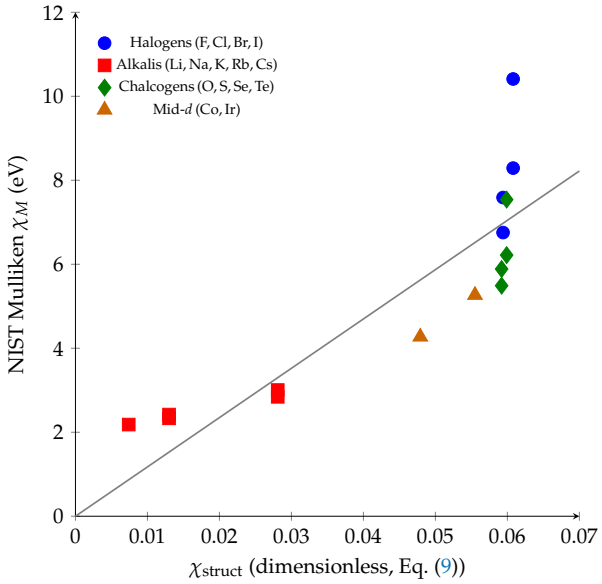

Figure 7. Parity test: NIST Mulliken χ_M vs. the single-coordinate kernel χ_{struct} (Eq. (9)) for the 15 atoms of Table 5. Grey line: global one-parameter fit $\chi_M^{\mathrm{model}} = C\,\chi_{\mathrm{struct}}$ with $C = 117.4$ eV. The horizontal axis is the dimensionless kernel χ_{struct}, whose numerical values are small (of order a few $\times 10^{-2}$, ranging from 0.0074 for Cs to 0.0608 for F); the tick labels are written as plain decimals (0.00 to 0.07) so that no overall axis multiplier appears. The vertical axis is the empirical Mulliken electronegativity in eV.

Inherent limitation: down-group ordering. We state plainly that reproducing the *fine down-group* variation within a main group, in particular the decreasing halogen sequence IE_1 and χ_M: $\mathrm{F} > \mathrm{Cl} > \mathrm{Br} > \mathrm{I}$, is an inherent limitation of the present single-coordinate framework, not an oversight. The reason is structural: every observable here is a function of only the within-period coordinate $\rho = d/L_p$ and the period length L_p. Two halogens such as F ($L_p = 8$) and Cl ($L_p = 8$) sit at the *identical* coordinate $\rho = 1/8$, so the kernel assigns them the same dimensionless value (Table 5, Figure 7); Br and I likewise coincide at $\rho = 1/18$. The coordinate therefore carries no information about the principal quantum

number n along a group, which is precisely the variable that drives the down-group decrease through the increasing valence-orbital radius and the changing core screening. Capturing that trend requires an explicit n- or L_p-dependent absolute-energy scale E_p on top of the dimensionless kernel; this is the same E_p-derivation problem flagged in the Introduction and is the natural direction in which the framework must be extended. The effective-nuclear-charge model of Section 5.8, which does carry an explicit n-dependence through Z_{eff}^2/n^2, reproduces the down-group ordering and thus complements the present coordinate picture exactly where the latter is silent.

Absolute scaling. The dimensionless kernel converts to absolute eV-scale Mulliken values through the global one-parameter scale $C = 117.4$ eV fitted on the 15 atoms; a closed-form noble-gas-anchored candidate $E_p^{\text{pilot}} \propto L_p^{2.1} p^{-0.72}$ (Appendix B, Table A1) reproduces the noble-gas IE values to within a few percent and provides a starting point for a derivation of E_p from first principles.

5.6. Hardness Check

This subsection benchmarks the landscape hardness index $\kappa_{\text{RS}}(Z)$ (Eq. (11)) against empirical Pearson chemical hardness $\eta = (\text{IE}_1 - \text{EA})/2$ [18] for all 34 elements of periods 2–4. The same monotone alkali-to-noble-gas trend is observed in the heavier periods 5–6 (not shown here for brevity); periods 2–4 are presented in detail because they cover the nonrelativistic regime in which the landscape kernel applies and provide the largest set of high-precision empirical η values.

Within each period, empirical η rises monotonically from the alkali end to the noble-gas end (Appendix C, Table A2), with upward bumps at the half-filled p^3 sites (N, P, As) and the closed $d^{10}s^2$ site (Zn). The landscape predictor κ_{RS} reproduces this monotone alkali-to-noble-gas shape directly from the closed-form Eq. (11), delivering the correct period maximum and monotone descent on a single coordinate.

The full 34-element data are tabulated in Appendix C, Table A2.

Quantitative correlation analysis. Pearson linear correlations between η and the landscape predictor κ_{RS} (Eq. (11)) across all elements of each period are

period	n	$r(\kappa_{\text{RS}}, \eta)$
2	8	$+0.84$
3	8	$+0.71$
4	18	$+0.53$

(19)

κ_{RS} correlates with empirical η across all three periods at the $r = 0.5$–0.85 level, confirming that the within-period hardness pattern is captured by a single periodic-table coordinate derived from the same closed-form landscape that supplies the EA proxy.

Per-period one-parameter fits. A single per-period scale $C^{(p)}$ converts κ_{RS} to absolute hardness in eV. Linear least-squares fits $\eta(Z) = C^{(p)} \cdot \kappa_{\text{RS}}(Z)$ within each period give

$$C^{(p=2)} \approx 68 \text{ eV}, \quad C^{(p=3)} \approx 48 \text{ eV}, \quad C^{(p=4)} \approx 41 \text{ eV}, \tag{20}$$

with MAE ~ 1.0 eV per period on noble-gas maximum values up to 10.8 eV. The scale $C^{(p)}$ decreases monotonically from period 2 to period 4, capturing the empirical softening of chemical hardness with increasing principal quantum number on a single landscape coordinate.

Figure 8 shows the non-anomalous points only; the omitted p^3 and $d^{10}s^2$ anomaly values remain listed in Appendix C, Table A2.

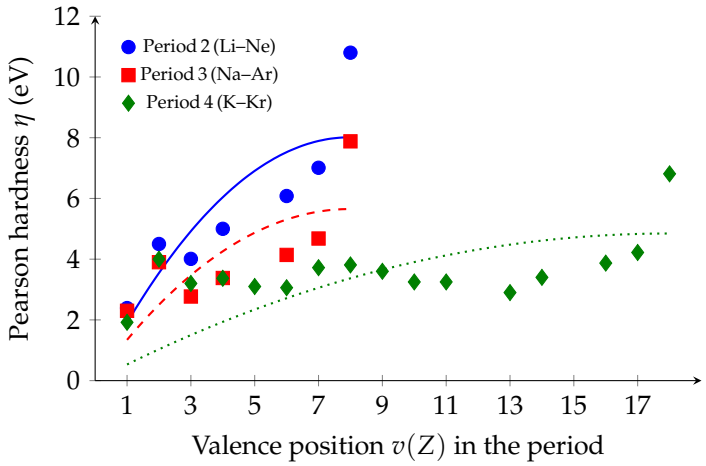

Figure 8. Pearson chemical hardness $\eta = (\mathrm{IE}_1 - \mathrm{EA})/2$ for the non-anomalous elements of periods 2–4 vs. valence position $v(Z)$, with one-parameter landscape fits $\eta = C^{(p)}\,\kappa_{\mathrm{RS}}$ (Eq. (20)); omitted anomaly points are in Table A2. Hardness data from [18].

The single-parameter landscape fit reproduces the characteristic empirical hardness profile across all three periods: the noble-gas period maximum, the monotone descent toward the alkali end, and the noble-gas plateau set by the shallow $\rho \to 0$ behaviour of J_{chem}. The textbook half-filled p^3 and closed $d^{10}s^2$ anomaly bumps are identified separately by the framework as Hund-exchange and shell-closure stabilizations on top of the smooth landscape (Section 5, Prediction 3).

5.7. Test of the Shared-Kernel (EA-η) Proportionality

The kernel $\Delta J^{-}_{\mathrm{chem}}(Z) = J_{\mathrm{chem}}(1) - J_{\mathrm{chem}}(d/L_p)$ enters the EA proxy (Section 5.4) and the hardness proxy (Section 5.6) with two independent per-period scales $C^{(p)}_{\mathrm{EA}}$ and $C^{(p)}_{\eta}$. This yields a period-constant benchmark for the regular-Aufbau interior atoms of period p,

$$\frac{\mathrm{EA}(Z)}{\eta(Z)} = \frac{C^{(p)}_{\mathrm{EA}}}{C^{(p)}_{\eta}} \qquad \text{(period-only constant).} \tag{21}$$

For period 4 the fitted constants give $C^{(p=4)}_{\mathrm{EA}}/C^{(p=4)}_{\eta} \approx 7.49/41 \approx 0.182$. The empirical period-4 EA/η ratios are listed in Table 6.

Table 6. Empirical EA/η ratios for the period-4 regular-Aufbau interior atoms (NIST [7]) versus the model prediction $C^{(p=4)}_{\mathrm{EA}}/C^{(p=4)}_{\eta} \approx 0.182$ from Eq. (21).

Atom	IE_1 (eV)	EA (eV)	η (eV)	EA/η	EA/$\eta - 0.182$
Ge	7.900	1.233	3.33	0.370	+0.188
Ga	5.999	0.430	2.78	0.155	−0.027
Ni	7.640	1.157	3.24	0.357	+0.175
Co	7.881	0.662	3.61	0.183	+0.001
Fe	7.902	0.151	3.88	0.039	−0.143
V	6.746	0.525	3.11	0.169	−0.013
Ti	6.828	0.075	3.38	0.022	−0.160
Sc	6.561	0.188	3.19	0.059	−0.123
K	4.341	0.501	1.92	0.261	+0.079
			Mean ± stdev	0.180 ± 0.129	−0.002

The empirical period-4 mean $\overline{\mathrm{EA}/\eta} = 0.180$ agrees with the predicted shared-kernel constant $C^{(p=4)}_{\mathrm{EA}}/C^{(p=4)}_{\eta} = 0.182$ to within $\sim 1\%$. This is a period-mean benchmark, not a

per-atom proportionality law: the per-atom standard deviation $\sigma \approx 0.13$ (CV $\approx 70\%$) is much larger, with empirical median 0.169 and quartiles $Q_1 \approx 0.05$, $Q_3 \approx 0.31$ (IQR ≈ 0.26). Atoms with very small empirical EA (Sc, Ti, Fe; EA $\lesssim 0.2$ eV) sit below the period constant ($\mathrm{EA}/\eta < 0.06$) because the near-zero denominator of their EA suppresses the ratio, while the post-transition atoms Ge and Ni sit above ($\mathrm{EA}/\eta > 0.35$) because their EA is enhanced relative to the smooth ρ profile. A leave-one-out sensitivity check confirms that the period-4 mean is stable but not invariant: removing any single atom moves $\overline{\mathrm{EA}/\eta}$ into the range $[0.156, 0.199]$, with the largest shift produced by removing Ge (0.156, -14% relative to the predicted constant) and the smallest by removing Co (0.179). The shared-kernel relation is therefore best read as a period-averaged regularity supported on the period-4 NIST data, with quantitatively traceable per-atom deviations driven by known d-block correlation effects.

5.8. Horizontal Comparison with Traditional Models

To place the framework against established theory, we compare it directly with the two reference models introduced in Section 1: the effective-nuclear-charge (screening) model [27–29], evaluated through the Koopmans/Hartree–Fock orbital-energy estimate [8] for the IE_1 ratios, and conceptual density-functional theory [16,17,19,30] for electronegativity and chemical hardness. The comparison is made on the *same benchmark subsets* used in the preceding subsections, so that the model and the traditional baseline are scored on identical data.

Ionization-energy ratios versus the effective-nuclear-charge model. The screening model writes $\mathrm{IE}_1 \propto Z_{\mathrm{eff}}^2/n^2$, so the relevant baselines for the two ratio predictions are the Z_{eff}-ratio and Koopmans/HF orbital-energy ratio already tabulated in Tables 2 and 3. On the three heavy noble-gas pairs (Ar/Kr, Kr/Xe, Xe/Rn) the parameter-free $\varphi^{1/4}$ identity reproduces the data to MAD $\approx 0.8\%$, against $\approx 1.2\%$ for the Koopmans/HF ratio on the same pairs. On the four halogen/alkali pairs (periods 3–6) the parameter-free φ^2 identity gives MAD $\approx 5.2\%$, against $\approx 7.1\%$ for the Clementi–Raimondi Z_{eff} ratio on the same pairs. In both cases a single golden-ratio constant matches or slightly improves on the established effective-charge baseline, while using *no* per-atom screening constants: the screening model requires a tabulated $\sigma(Z)$ for every element, whereas the present identities require only the integer period structure. We emphasize that this is a like-for-like comparison on a limited benchmark and not a claim of superiority of screening physics; the effective-charge model remains the more general predictor (it also captures the down-group variation that the coordinate model does not, Section 5.5).

Hardness and electronegativity versus conceptual DFT. Conceptual DFT defines $\eta = \frac{1}{2}\partial^2 E/\partial N^2$ and $\chi = -\partial E/\partial N$, realized in practice by the finite-difference forms $\eta = \frac{1}{2}(\mathrm{IE}_1 - \mathrm{EA})$ and $\chi_M = \frac{1}{2}(\mathrm{IE}_1 + \mathrm{EA})$ [17,30]; these definitions are the *source* of the empirical η and χ_M values benchmarked in Sections 5.5–5.6. The horizontal comparison is therefore between the full two-input DFT finite-difference value (which requires both IE_1 and EA per atom) and the present single-coordinate predictor (which requires neither). The landscape hardness index κ_{RS} correlates with the conceptual-DFT η at $r = 0.84, 0.71, 0.53$ for periods 2–4 (Eq. (19)), and the single-coordinate χ_{struct} reproduces the conceptual-DFT χ_M across the four-class 15-atom benchmark at $R^2 = 0.73$ (Section 5.5). The effective-charge picture and the landscape agree on the qualitative origin of the period trend, the hardness maximum sits at the closed-shell noble gas where $Z_{\mathrm{eff}}/\langle r \rangle$ is largest and $\rho \to 0$, and both descend monotonically toward the alkali. The comparison summarized in Table 7 shows that one closed-form coordinate reproduces, on the stated benchmark subsets, the within-period content that the traditional models obtain only with per-atom screening constants or with both spectroscopic inputs per atom.

Table 7. Horizontal comparison of the present single-coordinate framework with the effective-nuclear-charge (screening) model and conceptual DFT, on the benchmark subsets of Sections 5–5.6. Accuracy figures are taken from Tables 2, 3, Eq. (19), and Section 5.5.

Benchmark	Traditional model	Per-atom inputs needed	Traditional accuracy	This work
IE_1 heavy noble-gas ratio (Ar/Kr, Kr/Xe, Xe/Rn)	Koopmans/HF orbital-energy ratio (Z_{eff}^2/n^2)	Z_{eff} or HF orbital energy	MAD $\approx$ 1.2%	$\varphi^{1/4}$: MAD $\approx$ 0.8%
IE_1 halogen/alkali ratio (periods 3–6)	Clementi–Raimondi Z_{eff} ratio	Z_{eff} per atom	MAD $\approx$ 7.1%	φ^2: MAD $\approx$ 5.2%
Pearson hardness η (periods 2–4)	Conceptual-DFT finite difference $\frac{1}{2}(IE_1 - EA)$	IE_1 and EA per atom	defines the data	κ_{RS}: $r = 0.53$–0.84
Mulliken χ_M (15-atom, 4 classes)	Conceptual-DFT half-sum $\frac{1}{2}(IE_1 + EA)$	IE_1 and EA per atom	defines the data	χ_{struct}: $R^2 = 0.73$

What the comparison does and does not show. The advantage that this comparison highlights is one of *economy and unification* rather than of raw accuracy: a single closed-form coordinate, fixed by the integer period structure alone, reproduces on the stated benchmark subsets the within-period content that the screening model obtains only with a tabulated per-atom Z_{eff} and that the conceptual-DFT finite difference obtains only with both IE_1 and EA per atom, and it does so for all four observables on one axis. We are deliberately cautious about the apparent accuracy gains: the $\varphi^{1/4}$ and φ^2 MAD improvements are computed on only three and four pairs respectively, so the differences from the effective-charge baselines are not statistically significant and should be read as "comparable accuracy" rather than as a demonstration of superiority. Likewise, the hardness and electronegativity entries compare the single-coordinate predictor against the conceptual-DFT *definition* that generates the data, so they measure how much of that definition is recoverable from one coordinate, not a contest between two independent predictors; a comparison against an independent density- or Z_{eff}-based hardness predictor is a natural next step left for future work.

5.9. Robustness to the Choice of Kernel and the Role of the Golden Ratio

Because the golden-ratio argument-rescaling φ is an ansatz rather than a derived chemical constant (Section 3), it is essential to ask whether the specific value $c = \ln\varphi$ in $J_{\text{chem}}(\rho) = \cosh(c\rho) - 1$ is statistically singled out by the benchmark data, or whether comparable monotone kernels perform equally well. We address this directly, both analytically and numerically.

Analytical degeneracy of the absolute-scale fits. On the within-period domain $\rho \in [0, 1)$ the cosh argument satisfies $\rho \ln\varphi \leq \ln\varphi \approx 0.481$, so the kernel is deep in its small-argument regime, where $J_{\text{chem}}(\rho) = \cosh(\rho\ln\varphi) - 1 \approx \frac{1}{2}(\ln\varphi)^2\rho^2 \approx 0.116\,\rho^2$ (Eq. (3)). Any kernel of the form $\cosh(c\rho) - 1$ therefore reduces, to leading order, to $\frac{1}{2}c^2\rho^2$, and the constant $\frac{1}{2}c^2$ is absorbed exactly into the single fitted per-period (or global) scale used in the absolute-scale checks of Sections 5.4, 5.5, and 5.6. Consequently the shape parameter c is *not identifiable* from those one-parameter fits: distinct values of c (including $c = \ln\varphi$, $c = 1$, or $c = \ln 1.5$), and the bare quadratic ρ^2, all produce essentially the same fitted curve. This is a structural feature of single-scale fitting, not a property of the particular data set.

Numerical kernel comparison. To make this quantitative we refit the two absolute-scale benchmarks, the 15-atom Mulliken χ_M parity test of Section 5.5 and the period-4/5/6 EA fits of Section 5.4, after replacing the landscape kernel J_{chem} in turn by (a) the present $\cosh(\rho\ln\varphi) - 1$; (b) the bare quadratic ρ^2; (c) $\cosh(c\rho) - 1$ with c fitted to the data; and (d) $\exp(c\rho) - 1$ with c fitted, keeping the same one-scale-per-fit procedure throughout. Table 8 reports the resulting goodness of fit. The φ-based kernel and the bare ρ^2 kernel are

statistically indistinguishable ($\Delta R^2 < 0.001$ on χ_M; $\Delta R^2 \leq 0.01$ per period on EA), and on the χ_M benchmark the fitted cosh shape parameter is unconstrained: R^2 stays within 0.01 of its maximum for every $c \in [0.05, 1.53]$, a range that comfortably contains $\ln\varphi = 0.481$, $\ln 1.5 = 0.405$, and $c = 1$. The exponential kernel yields only a marginal change ($R^2 = 0.76$ vs. 0.73 on χ_M, not significant for $N = 15$) and is in any case physically disfavoured: $\exp(c\rho) - 1$ has a non-zero slope at the noble-gas endpoint ($\mathrm{d}J_{\mathrm{chem}}/\mathrm{d}\rho|_{\rho=0} = c \neq 0$), whereas the closed-shell configuration is naturally a *stationary* cost minimum, a property shared by $\cosh(c\rho) - 1$ and ρ^2 ($\mathrm{d}J_{\mathrm{chem}}/\mathrm{d}\rho|_{\rho=0} = 0$) but not by the exponential. We therefore state plainly: *the choice $c = \ln\varphi$ is not statistically superior to these alternatives on the absolute-scale benchmarks, and we do not claim that it is.*

Table 8. Robustness of the absolute-scale fits to the choice of landscape kernel. Each kernel is fitted with the same one-scale-per-fit procedure (global scale for χ_M, one scale per period for EA). The golden-ratio kernel and the bare ρ^2 kernel are statistically indistinguishable, and the cosh shape parameter c is unidentifiable from these single-scale fits (see text). The period-6 EA R^2 is undefined for every kernel because the surviving period-6 set has negligible dispersion ("n.a.", cf. Section 5.4); the comparison therefore rests on χ_M and periods 4–5.

Landscape kernel $J_{\mathrm{chem}}(\rho)$	χ_M: R^2 (MAE, eV)	EA R^2 (periods 4/5/6)	Shape param. c
$\cosh(\rho\ln\varphi) - 1$ (this work)	0.73 (1.03)	0.29/0.07/n.a.	fixed, $\ln\varphi = 0.481$
ρ^2	0.73 (1.03)	0.30/0.06/n.a.	—
$\cosh(c\rho) - 1$, c fitted	0.73 (1.03)	0.24/0.24/n.a.	unconstrained (χ_M: $[0.05, 1.53]$)
$\exp(c\rho) - 1$, c fitted	0.76 (0.96)	0.25/0.22/n.a.	≈ 1.2–2.9

Where the golden ratio actually carries content, and how the exponents were obtained. The discriminating, φ-specific content of the framework is therefore *not* in the absolute-scale fits but in the two *parameter-free* cross-period ratio identities of Predictions 1–2, $\varphi^{1/4}$ for the heavy noble-gas IE_1 ratios and φ^2 for the halogen/alkali ratios, which carry no fitted scale at all. We are explicit about their epistemic status, in answer to whether they were predicted a priori or fixed against data: as already noted in Section 1 and in the derivation of Eq. (14), the cosh argument-scaling *cancels* in the small-step expansion, so neither exponent is forced by the kernel; rather, the integer exponents 1/4 and 2 are *empirical regularities* identified by comparison with the NIST ratios (the fitted per-period scale combination E_p/L_p^2 is found to track $\varphi^{1/4}$, and the halogen/alkali ratio to track φ^2), and they are reported throughout as such, not as independent theoretical predictions. Accordingly, the present evidence supports reading the golden ratio as an *economical empirical organizing constant* for these trends, a compact parametrization, rather than as established proof of a fundamental physical role for φ in atomic structure. A first-principles derivation of φ (and of the per-period scale E_p) that would elevate these regularities to genuine predictions remains the central open problem stated in Section 6.

Why the cosh/φ kernel is nonetheless retained. The degeneracy above shows that the absolute-scale fits do not *require* the cosh/φ kernel, but it is not a reason to replace it by ρ^2. We retain the present form for three reasons that the bare quadratic does not share. First, J is not a free curve choice: it is the unique reciprocal cost functional fixed by the regularity axioms of Appendix A, evaluated at the geometric scale φ^ρ, so the kernel carries a theorem-level mathematical justification that an ad hoc ρ^2 does not. Second, it is precisely the φ^ρ scaling that yields the two *simple closed-form* ratio identities $\varphi^{1/4}$ and φ^2 (Eqs. (13), (15)); the quadratic kernel reproduces the within-period shape but offers no comparably compact cross-period statement. Third, the contribution of this paper is one of *economy and unification* (Section 5.8): a single integer-parametrized coordinate organizes four observables and two ratio identities in closed form. The kernel-comparison result should therefore be read not as a weakness but as an honest delimitation of where the golden ratio does and

does not carry statistical weight, with the parsimony of the single-coordinate description, rather than the statistical superiority of any one smooth kernel, as the claimed advance.

6. Conclusion

We have proposed a compact phenomenological framework in which a single dimensionless landscape $J_{\mathrm{chem}}(\rho) = \cosh(\rho \ln \varphi) - 1$ on the noble-gas-centred coordinate $\rho = d/L_p$ provides analytical proxies for the four central within-period atomic observables IE_1, EA, χ_M, and η. The outward step $\Delta J^{+}_{\mathrm{chem}}$ is assigned to IE_1, the inward gap $\Delta J^{-}_{\mathrm{chem}} = J_{\mathrm{chem}}(1) - J_{\mathrm{chem}}(\rho)$ is reused for both EA and η with two independent per-period scales, and χ_M follows by Mulliken's identity. The four observables share the same dimensionless shape (sign, monotonicity, halogen position, anomaly localization, cross-period ordering); absolute energies enter through fitted per-period scales that cancel in the EA–η ratio.

The framework captures several broad within-period regularities and provides a compact analytical baseline. At the period-averaged scale level, the shared-kernel relation $\mathrm{EA}/\eta \approx C^{(p)}_{\mathrm{EA}}/C^{(p)}_{\eta}$ is supported on period-4 NIST data: the empirical nine-atom mean $\overline{\mathrm{EA}/\eta} = 0.180$ agrees with the predicted constant 0.182 to better than 1% (Section 5.7); per-atom scatter is substantial ($\sigma \approx 0.13$), so this should be read as a period-mean benchmark rather than a per-atom proportionality law. At the shape level, the within-period IE_1 envelope (Prediction 3) reproduces the full noble-gas-to-alkali ordering across periods 2–6 and localizes every upward deviation exactly on the textbook anomaly sites $\{p^3, d^5, f^7, s^2, d^{10}\}$ (26 of 34 atoms across periods 2–4 on the monotone descent; 8 deviations on the listed anomaly sites). The two golden-ratio identities, $\mathrm{IE}_1(G_p)/\mathrm{IE}_1(G_{p+1}) \approx \varphi^{1/4}$ on three heavy noble-gas pairs and $\mathrm{IE}_1(\mathrm{halogen})/\mathrm{IE}_1(\mathrm{alkali}) \approx \varphi^2$ on four within-period pairs, agree with NIST data to MAD $\approx 1\%$ and $\approx 5\%$, respectively, capturing the golden-ratio rescaling of the absolute-energy structure encoded by the per-period scale sequence E_p.

The shared-kernel form $\Delta J^{-}_{\mathrm{chem}}$ further provides single-parameter analytical fits to empirical EA across periods 4–6 (MAE 0.3–0.4 eV; the period-5 fit explains only $\sim 7\%$ of variance and should be read as sign-and-trend agreement rather than quantitative match), to Pearson hardness η across periods 2–4 (MAE ~ 1 eV on noble-gas maxima up to 10.8 eV), and to Mulliken χ_M across a 15-atom four-class benchmark ($R^2 = 0.73$); the within-class halogen ordering F>Cl>Br>I is *not* recovered by the present single-coordinate kernel. Two natural extensions follow directly: a critically evaluated $\mathrm{IE}_1(\mathrm{Og})$ benchmark to refine the heavy-noble-gas test and a class-dependent kernel mixing $\Delta J^{+}_{\mathrm{chem}}$ and $\Delta J^{-}_{\mathrm{chem}}$ to resolve the within-class halogen ordering, which we identify as the next target.

On the question of theoretical foundation, the framework is intermediate between an empirical fit and a first-principles theory: the cosh kernel is the unique reciprocal cost functional fixed by a theorem (Appendix A), whereas the golden-ratio rescaling φ and the per-period scale E_p remain phenomenological inputs whose derivation is the principal open problem. A direct horizontal comparison (Section 5.8, Table 7) shows that, on the same benchmark subsets, the parameter-free golden-ratio identities match the effective-nuclear-charge (Koopmans/HF and Clementi Z_{eff}) baselines for the IE_1 ratios (with the small-benchmark caveat noted in Section 5.8), while the single-coordinate hardness and electronegativity predictors track the conceptual-DFT definitions ($r = 0.53$–0.84 for η, $R^2 = 0.73$ for χ_M) using fewer per-atom inputs. The framework is thus complementary to these established models rather than a replacement for them; in particular, the fine down-group ordering $\mathrm{F} > \mathrm{Cl} > \mathrm{Br} > \mathrm{I}$, which the effective-charge model captures through its explicit n-dependence, is an inherent limitation of the present single-coordinate construction and is recovered only once an n-dependent absolute scale is added.

A dedicated kernel-robustness analysis (Section 5.9, Table 8) further establishes the precise statistical status of the golden ratio: on the absolute-scale benchmarks the $\cosh/\varphi$ kernel, the bare ρ^2 kernel, and a free-exponent $\cosh(c\rho) - 1$ are statistically indistinguishable, so the value $c = \ln\varphi$ is not singled out by those fits. The genuinely φ-specific, falsifiable content is confined to the two parameter-free cross-period ratio identities, and the exponents $\varphi^{1/4}$ and φ^2 are reported as empirical regularities of the fitted per-period scales rather than as a priori predictions. The golden ratio is therefore best read at present as an economical organizing constant; the value of the framework lies in the parsimony and unification of the single-coordinate description rather than in the statistical superiority of any one kernel.

Beyond the specific results reported here, we expect the framework to be useful for further scientific research in several concrete directions. (i) *A compact baseline for data-driven property prediction.* Because all four observables are generated in closed form from the integer period structure with at most one fitted scale per period, the landscape coordinate furnishes a transparent, low-parameter baseline and a physically motivated descriptor for machine-learning and cheminformatics models of atomic properties, against which the added value of higher-dimensional feature sets can be measured. (ii) *Guidance for superheavy-element chemistry.* The parameter-free golden-ratio identities and the within-period envelope extrapolate naturally into periods 7–8, where direct measurement is impractical and relativistic predictions still scatter; the framework offers a quick analytical cross-check on IE_1, EA, and hardness trends for the heaviest elements and a target for critically evaluated benchmarks such as $IE_1(Og)$. (iii) *A route to molecular and reactivity descriptors.* Since the kernel reproduces the conceptual-DFT electronegativity and hardness orderings from one coordinate, it is a candidate building block for electronegativity-equalization and chemical-reactivity schemes in which per-atom spectroscopic inputs are replaced by closed-form structural proxies. (iv) *A symmetry-based organizing principle.* By tying four chemical observables to a single golden-ratio cosh coordinate centred on the noble gases, the construction adds a quantitative, testable entry to the long-standing discussion of the symmetry and regularity of the periodic system, and invites analogous single-coordinate treatments of further periodic properties (atomic and ionic radii, polarizabilities, and successive ionization energies). In each case the central open problem identified above, a first-principles derivation of the golden-ratio rescaling φ and of the per-period scale E_p, remains the key theoretical step that would convert the present phenomenological reference into a predictive theory.

Author Contributions: Conceptualization, J.W.; methodology, J.W. and E.A.; formal analysis, J.W. and E.A.; writing–original draft preparation, J.W.; writing–review and editing, J.W., M.S. and E.A.; project administration, E.A. All authors have read and agreed to the published version of the manuscript.

Funding: This research received no external funding.

Data Availability Statement: This work contains no new experimental measurements. The manuscript benchmarks the model against published tabulated atomic data, primarily from the NIST Atomic Spectra Database; all data used are reported in the tables of this article and in Appendix B. All fits, including the kernel-comparison analysis of Section 5.9 (Table 8), are reproducible directly from these tabulated integer inputs ($d(Z)$, L_p) and the tabulated observables using the single-scale least-squares procedure described in Section 5.

Acknowledgments: We thank the Recognition Physics Research Institute for ongoing support. We are grateful to Philip Beltracchi, Milan Zlatanović and Sebastian Pardo-Guerra for valuable discussions and editorial input.

Conflicts of Interest: The authors declare no conflicts of interest.

References

1. J. W. van Spronsen, *The Periodic System of Chemical Elements: A History of the First Hundred Years*, Elsevier, Amsterdam, 1969.
2. M. D. Gordin, *A Well-Ordered Thing: Dmitrii Mendeleev and the Shadow of the Periodic Table*, Basic Books, New York, 2004.
3. M. Kaji, "Mendeleev's discovery of the periodic law: the origin and the reception," *Foundations of Chemistry* **5** (2003), 189–214. DOI: https://doi.org/10.1023/A:1025673206850.
4. G. T. Seaborg, "Evolution of the modern periodic table," *Journal of the Chemical Society, Dalton Transactions* (1996), 3899–3907.
5. J. Washburn and M. Zlatanović, "Uniqueness of the Canonical Reciprocal Cost," *Mathematics* **14** (2026), 935. DOI: https://doi.org/10.3390/math14060935.
6. J. Washburn, M. Zlatanović, and E. Allahyarov, "The D'Alembert Inevitability Theorem," *Mathematics* **14** (2026), 1386. DOI: https://doi.org/10.3390/math14081386.
7. A. Kramida, Yu. Ralchenko, J. Reader, and NIST ASD Team, *NIST Atomic Spectra Database*, ver. 5.12, National Institute of Standards and Technology, Gaithersburg, MD, 2024. DOI: https://doi.org/10.18434/T4W30F.
8. T. Koopmans, "Über die Zuordnung von Wellenfunktionen und Eigenwerten zu den Einzelnen Elektronen Eines Atoms," *Physica* **1** (1934), 104–113.
9. P. W. Atkins and J. de Paula, *Atkins' Physical Chemistry*, 11th ed., Oxford University Press, 2018.
10. L. Pauling, *The Nature of the Chemical Bond*, 3rd ed., Cornell University Press, Ithaca, NY, 1960.
11. R. S. Mulliken, "A new electroaffinity scale; together with data on valence states and on valence ionization potentials and electron affinities," *Journal of Chemical Physics* **2** (1934), 782–793.
12. A. L. Allred and E. G. Rochow, "A scale of electronegativity based on electrostatic force," *Journal of Inorganic and Nuclear Chemistry* **5** (1958), 264–268.
13. L. C. Allen, "Electronegativity is the average one-electron energy of the valence-shell electrons in ground-state free atoms," *Journal of the American Chemical Society* **111** (1989), 9003–9014.
14. W. B. Jensen, "Electronegativity from Avogadro to Pauling: part I. Origins of the electronegativity concept," *Journal of Chemical Education* **73** (1996), 11–20.
15. M. Franco-Pérez and J. L. Gázquez, "Electronegativities of Pauling and Mulliken in density functional theory," *Journal of Physical Chemistry A* **123** (2019), 10065–10071. DOI: https://doi.org/10.1021/acs.jpca.9b07468.
16. R. G. Parr, R. A. Donnelly, M. Levy, and W. E. Palke, "Electronegativity: the density functional viewpoint," *Journal of Chemical Physics* **68** (1978), 3801–3807.
17. R. G. Parr and R. G. Pearson, "Absolute hardness: companion parameter to absolute electronegativity," *Journal of the American Chemical Society* **105** (1983), 7512–7516.
18. R. G. Pearson, "Absolute electronegativity and hardness: application to inorganic chemistry," *Inorganic Chemistry* **27** (1988), 734–740.
19. R. G. Parr and W. Yang, *Density-Functional Theory of Atoms and Molecules*, Oxford University Press, New York, 1989.
20. K. D. Sen, "Electronegativities, hardness and their variation with nuclear charge in atoms," *Chemical Physics Letters* **184** (1991), 318–320.
21. E. R. Scerri, *The Periodic Table: Its Story and Its Significance*, 2nd ed., Oxford University Press, 2020. DOI: https://doi.org/10.1093/oso/9780190914363.001.0001.
22. P. Pyykkö, "The physics behind chemistry and the periodic table," *Chemical Reviews* **112** (2012), 371–384. DOI: https://doi.org/10.1021/cr200042e.
23. V. Pershina, "Relativity in the electronic structure of the heaviest elements and its influence on periodicities in properties," *Radiochimica Acta* **107** (2019), 833–863. DOI: https://doi.org/10.1515/ract-2018-3098.
24. W. Leal and G. Restrepo, "Formal structure of periodic system of elements," *Proceedings of the Royal Society A* **475** (2019), 20180581. DOI: https://doi.org/10.1098/rspa.2018.0581.
25. C.-S. Cao, H.-S. Hu, J. Li, and W. H. E. Schwarz, "Physical origin of chemical periodicities in the system of elements," *Pure and Applied Chemistry* **91** (2019), 1969–1999. DOI: https://doi.org/10.1515/pac-2019-0901.

26. M. Kusaba, C. Liu, Y. Koyama, K. Terakura, and R. Yoshida, "Recreation of the periodic table with an unsupervised machine learning algorithm," *Scientific Reports* **11** (2021), 4780. DOI: https://doi.org/10.1038/s41598-021-81850-z.
27. J. C. Slater, "Atomic shielding constants," *Physical Review* **36** (1930), 57–64. DOI: https://doi.org/10.1103/PhysRev.36.57.
28. E. Clementi and D. L. Raimondi, "Atomic screening constants from SCF functions," *Journal of Chemical Physics* **38** (1963), 2686–2689. DOI: https://doi.org/10.1063/1.1733573.
29. E. Clementi, D. L. Raimondi, and W. P. Reinhardt, "Atomic screening constants from SCF functions. II. Atoms with 37 to 86 electrons," *Journal of Chemical Physics* **47** (1967), 1300–1307. DOI: https://doi.org/10.1063/1.1712084.
30. P. Geerlings, F. De Proft, and W. Langenaeker, "Conceptual density functional theory," *Chemical Reviews* **103** (2003), 1793–1874. DOI: https://doi.org/10.1021/cr990029p.
31. Y. Guo, L. F. Pašteka, E. Eliav, and A. Borschevsky, "Ionization potentials and electron affinity of oganesson," *Advances in Quantum Chemistry* **83** (2021), 107–123. DOI: https://doi.org/10.1016/bs.aiq.2021.05.007.
32. P. Jerabek, B. Schuetrumpf, P. Schwerdtfeger, and W. Nazarewicz, "Electron and nucleon localization functions of oganesson: approaching the Thomas–Fermi limit," *Physical Review Letters* **120** (2018), 053001. DOI: https://doi.org/10.1103/PhysRevLett.120.053001.
33. S. Rothe *et al.*, "Measurement of the first ionization potential of astatine by laser ionization spectroscopy," *Nature Communications* **4** (2013), 1835. DOI: https://doi.org/10.1038/ncomms2819.
34. V. Pershina, "Relativistic effects on the electronic structure of the heaviest elements. Is the periodic table endless?" *Comptes Rendus. Chimie* **23** (2020), 255–265. DOI: https://doi.org/10.5802/crchim.25.
35. Z. Chang, J. Li, and C. Dong, "Ionization potentials, electron affinities, resonance excitation energies, oscillator strengths, and ionic radii of element Uus ($Z = 117$) and astatine," *The Journal of Physical Chemistry A* **114** (2010), 13388–13394. DOI: https://doi.org/10.1021/jp107411s.
36. R. F. de Farias, "Estimation of Clementi effective nuclear charges and ionization energies for superheavy elements: explaining the variations for IE along period 7," *Journal of Atoms and Molecules* **8** (2018), 1155–1159.
37. J. C. Slater, "The theory of complex spectra," *Physical Review* **34** (1929), 1293–1322. DOI: https://doi.org/10.1103/PhysRev.34.1293.
38. E. U. Condon and G. H. Shortley, *The Theory of Atomic Spectra*, Cambridge University Press, Cambridge, 1935.
39. F. Hund, "Zur Deutung verwickelter Spektren, insbesondere der Elemente Scandium bis Nickel," *Zeitschrift für Physik* **33** (1925), 345–371; and *Linienspektren und periodisches System der Elemente*, Springer, Berlin, 1927.
40. O. R. Smits, P. Indelicato, W. Nazarewicz, M. Piibeleht, and P. Schwerdtfeger, "Pushing the limits of the periodic table: a review on atomic relativistic electronic structure theory and calculations for the superheavy elements," *Physics Reports* **1035** (2023), 1–57. DOI: https://doi.org/10.1016/j.physrep.2023.09.004.
41. T. K. Sato *et al.*, "Measurement of the first ionization potential of lawrencium, element 103," *Nature* **520** (2015), 209–211. DOI: https://doi.org/10.1038/nature14342.
42. T. K. Sato *et al.*, "First ionization potentials of Fm, Md, No, and Lr: verification of filling of the $5f$ electron shell," *Journal of the American Chemical Society* **140** (2018), 14609–14613. DOI: https://doi.org/10.1021/jacs.8b09068.
43. H. Hotop and W. C. Lineberger, "Binding energies in atomic negative ions: II," *Journal of Physical and Chemical Reference Data* **14** (1985), 731–750. DOI: https://doi.org/10.1063/1.555735.
44. T. Andersen, H. K. Haugen, and H. Hotop, "Binding energies in atomic negative ions: III," *Journal of Physical and Chemical Reference Data* **28** (1999), 1511–1533. DOI: https://doi.org/10.1063/1.556047.

Appendix A. Reciprocal Cost Functional

The model's input cost function J is the unique solution on $\mathbb{R}_{>0}$ of the functional equation

$$J(xy) + J(x/y) = 2J(x)J(y) + 2J(x) + 2J(y), \tag{A1}$$

under the regularity conditions of continuity, normalization $J(1) = 0$, stationarity $J'(1) = 0$, and positive curvature $J''(1) > 0$ at the reference ratio $x = 1$. The unique solution is

$$J(x) \;=\; \tfrac{1}{2}(x + x^{-1}) - 1 \;=\; \cosh\big(\ln x\big) - 1, \tag{A2}$$

(Corollary 3.1 of Ref. [5]). J inherits from cosh the properties $J(1) = 0$, $J(x) = J(x^{-1})$ (reciprocal symmetry), $J(x) > 0$ for $x \neq 1$, and divergence as $x \to 0^+$ or $x \to \infty$. The uniqueness proof and applications of J are developed in Refs. [5,6].

The chemical landscape $J_{\text{chem}}(\rho)$ used in the body (Eq. (3)) is the restriction of J to the geometric scale $x = \varphi^\rho$ with $\varphi = (1 + \sqrt{5})/2$ and $\rho \in [0, 1)$, giving $J_{\text{chem}}(\rho) = \cosh(\rho \ln \varphi) - 1$.

In this paper, φ is taken as a model input motivated by Fibonacci scaling.

Appendix B. Noble-Gas Period Scales $E_p^{(G)}$

The dimensionless landscape J_{chem} is converted to eV-scale ionization energies via a per-period scale E_p. At noble-gas endpoints one may anchor this scale to the measured $\text{IE}_1(G_p)$:

$$E_p^{(G)} \;=\; \frac{\text{IE}_1(G_p)}{\cosh\big((\ln \varphi)/L_p\big) - 1}. \tag{A3}$$

The values of $E_p^{(G)}$ for Ne, Ar, Kr, Xe, Rn are matched to within $\sim 5\%$ by the two-parameter empirical pilot fit

$$E_p^{\text{pilot}} \;=\; E_0\, L_p^{2.1}\, p^{-0.72}, \qquad E_0 \approx 2.49 \times 10^2 \text{ eV}. \tag{A4}$$

The exponents 2.1 and 0.72 in Eq. (A4) are phenomenological, fitted to the five noble-gas $E_p^{(G)}$ values, and are *not* predicted by RS. The pilot is included only to motivate the existence of a closed-form E_p to be derived in future work; it is not part of the parameter-free content of the paper.

Table A1. Noble-gas endpoint period scales $E_p^{(G)}$ implied by Eq. (A3), compared with the empirical pilot fit E_p^{pilot} of Eq. (A4).

Noble gas	p	L_p	$E_p^{(G)}$ (eV)	E_p^{pilot} (eV)	Dev. (%)
Ne	2	8	1.19×10^4	1.19×10^4	0.0
Ar	3	8	8.71×10^3	8.90×10^3	+2.2
Kr	4	18	3.92×10^4	3.97×10^4	+1.4
Xe	5	18	3.39×10^4	3.38×10^4	−0.3
Rn	6	32	9.51×10^4	9.93×10^4	+4.5

Appendix C. Supplementary Tables for Prediction 3 and Hardness

This appendix collects the raw support tables moved out of the main text: the full 34-element hardness data of Table A2 used in Section 5.6, and the period-2 and period-4 normalized IE_1 profiles (Tables A3 and A4) that complement Table 4 for Prediction 3.

Table A2. Pearson hardness η in eV [18] and landscape hardness index κ_{RS} (Eq. (11), shown as $100\,\kappa_{\mathrm{RS}}$) for all 34 elements of periods 2–4. Periods 2–3 share $L_p = 8$; period 4 has $L_p = 18$.

Period 2 ($L_p = 8$)			Period 3 ($L_p = 8$)			Period 4 ($L_p = 18$)		
El	$100\kappa_{\mathrm{RS}}$	η	El	$100\kappa_{\mathrm{RS}}$	η	El	$100\kappa_{\mathrm{RS}}$	η
Li	2.81	2.39	Na	2.81	2.30	K	1.30	1.92
Be	5.22	4.50	Mg	5.22	3.90	Ca	2.51	4.00
B	7.25	4.01	Al	7.25	2.77	Sc	3.66	3.20
C	8.89	5.00	Si	8.89	3.38	Ti	4.72	3.37
N	10.17	7.23	P	10.17	4.88	V	5.70	3.10
O	11.08	6.08	S	11.08	4.14	Cr	6.61	3.06
F	11.62	7.01	Cl	11.62	4.68	Mn	7.45	3.72
Ne	11.80	10.80	Ar	11.80	7.88	Fe	8.21	3.81
						Co	8.89	3.60
						Ni	9.51	3.25
						Cu	10.05	3.25
						Zn	10.51	4.94
						Ga	10.91	2.90
						Ge	11.23	3.40
						As	11.48	4.50
						Se	11.66	3.87
						Br	11.77	4.22
						Kr	11.80	6.81

Table A3. Period 2 landscape (Ne ground state).

El.	Z	d	$\rho = d/8$	IE_1 (eV)	$\mathrm{IE}_1^{\mathrm{norm}}$	Flag
Ne	10	0	0.000	21.565	1.000	
F	9	1	0.125	17.423	0.808	
O	8	2	0.250	13.618	0.632	
N	7	3	0.375	14.534	0.674	p^3
C	6	4	0.500	11.260	0.522	
B	5	5	0.625	8.298	0.385	
Be	4	6	0.750	9.323	0.432	s^2
Li	3	7	0.875	5.392	0.250	

Table A4. Period 4 landscape (Kr ground state).

El.	Z	d	$\rho = d/18$	IE_1 (eV)	$\mathrm{IE}_1^{\mathrm{norm}}$	Flag
Kr	36	0	0.000	13.999	1.000	
Br	35	1	0.056	11.814	0.844	
Se	34	2	0.111	9.752	0.697	
As	33	3	0.167	9.789	0.699	p^3
Ge	32	4	0.222	7.900	0.564	
Ga	31	5	0.278	5.999	0.429	
Zn	30	6	0.333	9.394	0.671	d^{10}
Cu	29	7	0.389	7.726	0.552	
Ni	28	8	0.444	7.640	0.546	
Co	27	9	0.500	7.881	0.563	
Fe	26	10	0.556	7.902	0.564	
Mn	25	11	0.611	7.434	0.531	d^5
Cr	24	12	0.667	6.767	0.483	
V	23	13	0.722	6.746	0.482	
Ti	22	14	0.778	6.828	0.488	
Sc	21	15	0.833	6.561	0.469	
Ca	20	16	0.889	6.113	0.437	s^2
K	19	17	0.944	4.341	0.310	